Thermal Consideration and Design for a 200-kW SiC-Based High-Density Three-Phase Inverter in More Electric Aircraft

Che-Wei Chang, *Graduate Student Member, IEEE*, Xingchen Zhao, *Graduate Student Member, IEEE*, Ripun Phukan, *Member, IEEE*, Rolando Burgos, *Senior Member, IEEE*, Simon Uicich, Pascal Asfaux, and Dong Dong, *Senior Member, IEEE*

***Abstract*— As advances in semiconductor, dielectric, and magnetic materials enhance the power density of power conversion systems, the emphasis on efficient cooling solutions becomes paramount. Effective thermal management is vital as it directly influences the power density and reliability of power inverters. This is especially crucial for high-altitude motor drives, given the challenges posed by reduced air density. This article provides a design process of thermal management for high-density high-power inverters. Thermal models for different scenarios are derived, and the hotspot temperature can be estimated under different cooling conditions. To demonstrate the proposed design process, a 200-kW three-level T-type propulsion inverter designed for an altitude of 7620 m (25 000 ft) is used to present the thermal designs. Several thermal mitigation techniques are also introduced. A critical finding is the potential for stagnating air spaces to produce localized hotspots in areas such as the busbar, gate-driver boards, and terminals. Historically, these hotspots have been overlooked, yet they can significantly degrade overall thermal performance and system reliability. To address the thermal issue of hotspots caused by stagnating air space, several solutions are proposed. Of these, the localized forced cooling air duct (AD) solution is selected in this work. By optimizing both internal and external airflows, the hotspot temperature in the stagnating air space is reduced by 37% using the designed AD without oversizing the overall cooling system. Moreover, based on full-power experimental thermal tests, we demonstrate that the inverter's hotspot temperature within a sealed enclosure can be kept below 130 °C in an environment of 75 °C and at an altitude of 7620 m. The culmination of our research validates the efficacy of the proposed design process.**

***Index Terms*— High density, high power, more electric aircraft (MEA), propulsion inverters, thermal management.**

Manuscript received 4 May 2023; revised 6 July 2023 and 7 August 2023; accepted 8 August 2023. Date of publication 25 August 2023; date of current version 1 December 2023. This work was supported by Airbus, France. Recommended for publication by Associate Editor Debaprasad Kastha. *(Corresponding author: Che-Wei Chang.)*

Che-Wei Chang, Xingchen Zhao, Rolando Burgos, and Dong Dong are with the Center for Power Electronics Systems (CPES), Department of Electrical and Computer Engineering, Virginia Polytechnic Institute and State University, Blacksburg, VA 24061 USA (e-mail: cwchang@vt.edu).

Ripun Phukan is with the Delta Power Electronics Laboratory, Delta Electronics, Raleigh, NC 27709 USA.

Simon Uicich and Pascal Asfaux are with Electronics Department, Airbus Operations SAS, 31300 Toulouse, France.

Color versions of one or more figures in this article are available at https://doi.org/10.1109/JESTPE.2023.3308854.

Digital Object Identifier 10.1109/JESTPE.2023.3308854

I. Introduction

HYBRID and full electric propulsions have emerged as leading contenders for reducing exhaust emissions [1]. Power electronic drives that spin the motor-fan propulsor need to deliver high efficiency and high power density. Silicon-carbide (SiC) power devices provide a promising performance to achieve these targets compared to conventional silicon (Si) devices [2], [3], [4], [5]. Combined with multilevel inverter topology, the propulsion drive features low switching loss and low electromagnetic interference (EMI) noise [6], [7]. However, as power electronics become more compact, thermal challenges arise due to elevated heat flux. These thermal issues can lead to system failures, such as component cracks, solder joint fatigue, and wire liftoffs [8], [9]. In high altitudes, the harsh environment worsens the thermal conditions because of the decreased air density [10], [11], [12], [13].

Efficient thermal management aims to keep all hotspot temperatures within safe limits in power inverters. To cool power devices, single-phase cooling using coolants of air or water mixtures is the most popular. However, in traction or propulsion systems, the inverters are often housed in sealed enclosures for safety reasons, which makes it challenging for conventional air cooling to meet the cooling requirements [14], [15], [16], [17], [18]. The cooling capability of conventional forced air cooling is usually lower than 50 W/cm^2 [19], [20] and is insufficient to meet cooling demand for high-power devices especially when the total loss exceeds 1500 W [21]. To address the cooling demand of higher power dissipation, microchannel liquid cooling (MLC), which has a cooling capability higher than 100 W/cm^2, has become a widely adopted solution in power inverters due to its industry maturity, low weight, and low cost [15]. Researchers have conducted studies to optimize the thermal performance of MLC [22], [23], [24], [25], [26], [27], [28], [29]. The results indicate that the cooling capacity of MLC is significantly influenced by factors such as channel geometry, fluid characteristics, and coolant path configuration [30], [31], [32], [33].

The cooling capability of the system can be enhanced by using a coolant with higher thermal conductivity, such as a metal liquid coolant. This approach has been shown to reduce the temperature rise by 38% [34]. In addition,

recent studies have demonstrated the benefits of reduced pump power consumption compared to water-based pumps [35]. The combination of metal liquid coolant and MLC has been demonstrated to achieve cooling capacities greater than 1000 W/cm^2 [36]. Another advanced single-phase cooling technique, jet impingement liquid cooling, can offer cooling capability ranging from 200 to 1000 W/cm^2 [37]. The cooling capacity of this method is largely impacted by nozzle design [23], [38], [39], [40], [41], [42]. Although jet impingement has been utilized in some applications [43], [44], [45], it is not commonly adopted in electric vehicles (EVs) or high-altitude more electric aircraft (MEA) due to its higher pressure drop and complex structure [23]. The risk of coolant leakage between the device and the cooling chamber also renders it unsuitable for high-altitude MEA applications.

Two-phase cooling technologies, such as vapor chambers, offer cooling capabilities beyond 1000 W/cm^2. The technique leverages the fluid phase change transition and exhibits higher heat transfer efficiency and excellent heat spreading performance, making it ideal for applications with limited space constraints [46], [47], [48], [49]. The vapor chamber can also be utilized as a substitute for traditional copper baseplate of MLC to reduce thermal resistance and improve temperature distribution. A study [50] demonstrated that the maximum temperature can be reduced by 26% and temperature distribution improved. Furthermore, an ultrathin vapor chamber with a thickness of 0.4 mm has been found to possess thermal conductivity 30 times greater than that of a pure copper baseplate [51].

Recently, researchers have focused on eliminating the thermal interface material (TIM) layer by integrating the cooling device into the device package or housing [52], [53]. Studies [54] and [55] have demonstrated that incorporating MLC into an aluminum nitride (AlN)-layer in the direct bond copper (DBC) layer reduces thermal resistance by 80%. This concept has also been utilized in some EVs for power devices [56]. The MLC has also been embedded in a printed circuit board (PCB) to cool chips [57]. A vapor chamber baseplate with a DBC substrate integrated into power modules was presented in [58], resulting in a 40% improvement in total loop thermal resistance. Double-side cooling has been demonstrated for a 10-kV SiC MOSFET module [59], [60], achieving a cooling capability higher than 250 W/cm^2. A comprehensive comparison of single-side cooling for different PCB technologies for power dies embedded in a PCB was recently published in [61], and double-side cooling for embedded die PCBs was also shown to result in a 57% reduction in junction-to-case thermal resistance compared to TO-247 devices [62].

Effective cooling of components beyond power devices is also a focus of research to mitigate localized hotspots. A thermal model for PCB-winding-based transformers is proposed and shows accuracy [63]. In [64], an air-cooling duct is designed to cool planar transformer windings. By optimizing the cooling airflow, the peak winding temperature is reduced by 8%, and the power consumption is four times smaller than that without airflow optimization. Similarly, Ruan et al. [65] utilized forced air cooling for the PCB-winding of transformers, reducing hotspot temperatures by 40%. The combination of forced air and phase change heat pipe has also been applied to cool transformer, as described in [66] and [67]. A liquid cooling chamber was designed for 50-kW filters in high-altitude applications in [68]. This approach was also utilized to cool EMI filters, as shown in [69].

Though cooling has been done for individual components in high-density power electronics inverters, a systematical thermal design process is missing in the literature. This article aims to provide a design process for thermal management. After all, optimal electrical design can only be achieved by having good thermal performance. The outline of this article is given as follows. In Section II, comprehensive thermal modeling, high-altitude impact, and proposed thermal design process are introduced. Section III presents the demonstrated 200-kW three-level (3-L) T-type inverter with its specifications. Thermal mitigation strategies and design for localized heat sources are also shown. Following the design workflow, the cooling design for SiC power modules is conducted in Section IV. Then, Section V discusses the thermal impact of stagnating air space and the proposed air-cooling duct solution with airflow optimization. All thermal designs are verified by experimental results shown in Section VI. Finally, Section VII draws the main conclusions.

II. Thermal Modeling and Thermal Design Process

Before establishing the design process of thermal management, a proper thermal model should be built to understand heat transfer. In all cases, the heat source temperature T_{hs} in power inverters can be impacted by factors listed as follows:

1) heat source;
2) heat transfer form;
3) heat transfer path;
4) ambient environment or cooling condition.

In a thermal system, the heat flux dissipated from a heat source will always seek a path to transfer to the lowest temperature. This temperature is usually determined by the ambient environment or cooling conditions. Multiple paths may exist for heat dissipation, and each path may involve various forms of heat transfer, such as conduction between solids, convection between solid and fluid, and radiation between surfaces. The specific form and path of heat transfer vary depending on the situation. However, all cases can be described by using a thermal resistance R_{th} network.

A. Modeling of Thermal Path With Passive Cooling

Fig. 1 illustrates the simplest thermal structure, wherein a heat source with passive cooling is located inside a sealed enclosure. For the purpose of analysis, the heat source can be assumed to have a rectangular body. $T_{enc,int}$ and $T_{enc,ext}$ denote the temperatures of the internal and external sides of the enclosure, respectively. To model this structure, the generated heat q is transferred from T_{hs} to the ambient temperature T_{amb} through events in categories of the following:

1) T_{hs} to heat source surface $T_{hs,surf}$ by conduction;
2) $T_{hs,surf}$ to internal air $T_{air,int}$ by convection;
3) $T_{air,int}$ to T_{amb} by heat exchange;
4) $T_{hs,surf}$ to $T_{enc,int}$ and $T_{enc,ext}$ to T_{amb} through radiation.

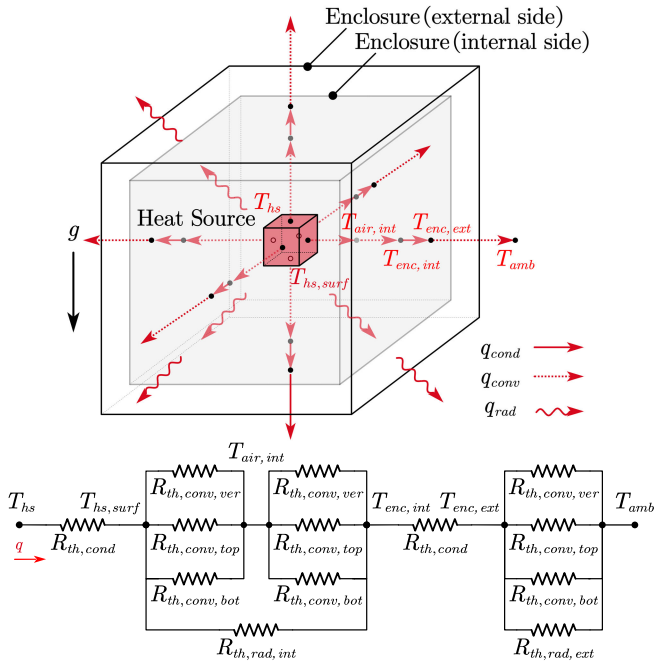

Fig. 1. Thermal structure and thermal resistance network when a heat source within a sealed enclosure dissipates the heat via natural convection.

The first event involves sole conduction through the heat source body, which may consist of various conduction paths such as die bonding, lead frame, device package, PCB, and thermal via. The conduction thermal resistance $R_{\text{th,cond}}$ can be expressed as

$$R_{\text{th,cond}} = \frac{L_{\text{cond}}}{k_{\text{cond}} \cdot A_{\text{cond}}} \tag{1}$$

where L_{cond}, k_{cond}, and A_{cond} are the thickness, thermal conductivity, and area of the solid, respectively. In the second event, the heat is transferred by convection, as shown in the dashed arrow in Fig. 1. By defining the $T_{\text{air,int}}$ as the average bulk temperature of internal air, the convective thermal resistance $R_{\text{th,conv}}$ can be written as

$$R_{\text{th,conv}} = \frac{1}{h_{\text{conv}} \cdot A_{\text{conv}}} \tag{2}$$

where h_{conv} is the convective heat transfer coefficient

$$h_{\text{conv}} = \frac{k_{\text{air}}}{L_c} \cdot Nu \tag{3}$$

where A_{conv} is the convection area, k_{air} is the conductivity of the air, and L_c is the characteristic length which is defined as

$$L_c = \frac{A_{\text{conv}}}{P} \tag{4}$$

where P is the perimeter of the object's surface. Nu in (3) is the Nusselt number. For the case of natural convection, the correlation of Nu is impacted by the directions of convection. By assuming that all six surfaces of the heat source are flat surfaces, the empirical Nu for top, bottom, and vertical surfaces can be derived as [70], [71]

$$Nu_{\text{top}} = \begin{cases} 0.54(\text{GrPr})^{1/4} 10^4 < \text{GrPr} < 10^7 \\ 0.15(\text{GrPr})^{1/3} 10^7 < \text{GrPr} < 10^{11} \end{cases} \tag{5}$$

$$Nu_{\text{bot}} = 0.27(\text{GrPr})^{1/4} 10^5 < \text{GrPr} < 10^{11} \tag{6}$$

$$Nu_{ver} = \begin{cases} \left\{ 0.825 + \dfrac{0.387(\text{GrPr})^{1/6}}{\left[1 + (0.492/\text{Pr})^{9/16}\right]^{8/27}} \right\}^2 \\ 0.68 + \dfrac{0.67(\text{GrPr})^{1/4}}{\left[1 + (0.492/\text{P r})^{9/16}\right]^{4/6}} \text{GrPr} \leqslant 10^9 \end{cases} \tag{7}$$

where Gr is the Grashof number that describes the ratio between buoyancy to viscous forces acting on air and Pr is the Prandtl number that defines the ratio of momentum diffusivity and thermal diffusivity. It is clear that Nu_{top} is the highest due to the nature of fluid mechanics, leading to a higher h_{conv} at the top surface compared to bottom and vertical surfaces. Gr and Pr in (5)–(7) can be expressed as

$$Gr = \frac{g \cdot \beta \cdot {L_c}^3 \left(T_{\text{hs,surf}} - T_{\text{air,int}}\right)}{\nu^2} \tag{8}$$

$$\text{Pr} = \frac{C_\rho \cdot \mu}{k_{\text{air}}} = \frac{C_\rho \cdot \rho \cdot \nu}{k_{\text{air}}} \tag{9}$$

where g is the gravitational acceleration, β is the thermal expansion coefficient, and ν is the kinematic viscosity. C_ρ is the specific heat, μ is the dynamic viscosity, and ρ is the fluid density.

The mechanism of the third event can be understood through the analogy of a heat exchanger, in which two fluids are separated by a solid that facilitates heat exchange between them. The solid can be assumed to be a flat, clean, and unfinned surface composed of a single material. Therefore, the R_{th} components in the third event consist of two $R_{\text{th,conv}}$'s in series with one $R_{\text{th,cond}}$ in the middle of them. In addition, the third event is in series with the first and second events.

For the final event, heat can also be transferred through radiation without any interaction with air. Unlike conduction and convection, radiation does not require a medium and is most efficient in a vacuum. Radiation can also occur between two bodies separated by a medium at a temperature colder than both bodies. Therefore, an additional path for radiation appears between two surfaces and is in parallel with the previous events. Assuming that the heat source within the enclosure is one enclosed system, with radiation $q_{\text{rad,int}}$, while the enclosure surrounded by external isothermal ambient is another enclosed system with $q_{\text{rad,ext}}$, the equations can be written by obeying Kirchhoff's law

$$q_{\text{rad, int}} = \frac{\sigma \cdot \left({T_{\text{hs,surf}}}^4 - {T_{\text{enc,int}}}^4\right)}{\frac{1-\varepsilon_{\text{hs}}}{\varepsilon_{\text{hs}} \cdot A_{\text{hat}}} + \frac{1}{A_{\text{hs}} \cdot F_{\text{hs-enc}}} + \frac{1-\varepsilon_{\text{enc}}}{\varepsilon_{\text{enc}} \cdot A_{\text{cnc,nat}}}} \tag{10}$$

$$q_{\text{rad,ext}} = \frac{\sigma \cdot \left({T_{\text{enc, ext}}}^4 - {T_{\text{amb}}}^4\right)}{\frac{1-\varepsilon_{\text{enc}}}{\varepsilon_{\text{enc}} \cdot A_{\text{enc, ext}}} + \frac{1}{A_{\text{enc, est}} \cdot F_{\text{enc-air}}} + \frac{1-\varepsilon_{\text{amb}}}{\varepsilon_{\text{amb}} \cdot A_{\text{amb}}}} \tag{11}$$

where σ is Stefan–Boltzmann's constant, ε is the emissivity of the material based on its radiative property, and F is the view factor which depends on the geometry. For the second enclosed system, since the area of ambient air A_{amb} can be

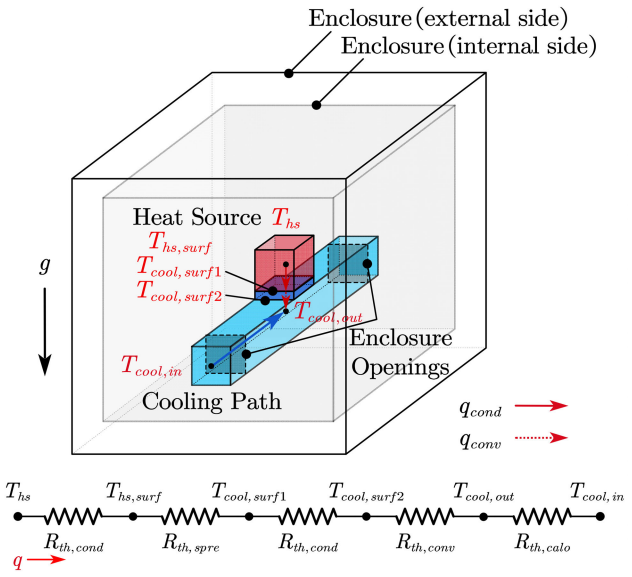

Fig. 2. Thermal structure and corresponding R_{th} network when the forced or active cooling method is adopted for the heat source.

assumed to be infinite, and $F_{\text{enc,ext}-\text{amb}}$ equals 1, then (11) can be simplified as

$$q_{\text{rad, ext}} \approx \varepsilon_{\text{enc}} \cdot A_{\text{enc, ext}} \cdot \sigma \cdot \left(T_{\text{enc,ext}}{}^4 - T_{\text{amb}}^4\right). \quad (12)$$

It is observed that the radiation transfer is positively related to temperature, while the temperature dependence of convective h_{conv} is usually weak. The radiative thermal resistance $R_{\text{th,rad}}$ is

$$R_{\text{th, rad}} = \frac{\Delta T}{q_{\text{rad}}}. \quad (13)$$

Finally, by combining (1)–(13), the corresponding R_{th} network for Fig. 1 can be depicted. The model is valid when assumptions are made as follows.

1) The system reaches a steady state.
2) The surfaces are isothermal.
3) The surfaces are gray bodies (emissivity = absorptivity), opaque (transmissivity = 0), and diffuse.
4) The radiation is uniform on each surface.

The model in Fig. 1 illustrates the mechanism of heat transfer from the heat source to the ambient. The steady state T_{hs} requires an iterative process for results to converge, which can be easily implemented in computing software, such as MATLAB.

B. Modeling of Thermal Path With Active Cooling

If the cooling solutions, such as forced air or liquid cooling, are adopted to cool components with high heat flux, the thermal scenario is described in Fig. 2. The heat source inside the enclosure is attached to the cooling device, such as a heat sink or cold plate. The cooling path aims to bring heat to the ambient or external system. To model the structure, the mechanism is summarized as in the following events:

1) T_{hs} to $T_{\text{hs,surf}}$ through conduction;
2) $T_{\text{hs,surf}}$ to $T_{\text{cool,surf1}}$ to $T_{\text{cool,surf2}}$ through spreading and conduction;
3) $T_{\text{cool,surf2}}$ to $T_{\text{cool,out}}$ through convection;
4) temperature rise between inlet $T_{\text{cool,in}}$ and outlet $T_{\text{cool,out}}$.

Similarly, the first event involves conduction from T_{hs} to $T_{\text{hs,surf}}$. In the second event, heat spreads from $T_{\text{hs,surf}}$ to $T_{\text{cool,surf1}}$ due to area mismatch, followed by conduction from $T_{\text{cool,surf1}}$ to $T_{\text{cool,surf2}}$, which contacts the cooling path. If the cooling device area is designed to be the same or similar to the heat source area, the spreading thermal resistance $R_{\text{th,spre}}$ can be negligible [72]. In the third event, the general expression is given in (2). The value of h_{conv} varies depending on the cooling techniques and requires empirical study. For the final event, $R_{\text{th,calo}}$ can be expressed as [73]

$$R_{\text{th, calo}} = \frac{1}{2 \cdot \dot{m} \cdot C_{\rho}} \quad (14)$$

where $\dot{m}$ is the mass flow rate and $R_{\text{th,calo}}$ is usually a much smaller fraction of the total R_{th}. Based on the above equations, the R_{th} network is illustrated in Fig. 2 with assumptions.

1) The natural convection and radiation from the heat source to the ambient are neglected since they are much larger than the branch of the active cooling path.
2) The fluid temperature is considered the average bulk temperature of the fluid.

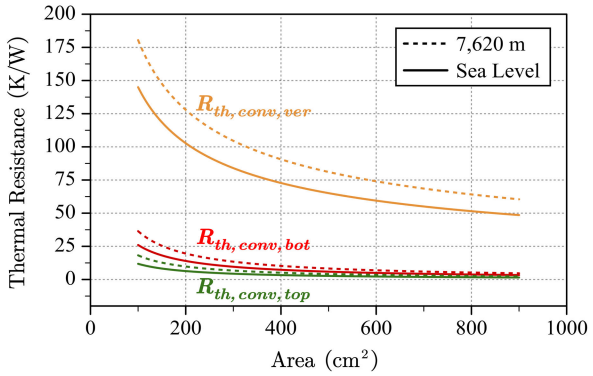

Fig. 3. Calculated $R_{\text{th,conv}}$ for top, bottom, and vertical surfaces at an ambient of 75 °C and an altitude of 7620 m based on parameters in Table I.

TABLE I
PARAMETERS OF 75 °C AIR AT DIFFERENT ALTITUDES

Parameters	Sea Level	7,620 m
Thermal Conductivity k_{air}	0.029 W/m·K	0.029 W/m·K
Gravitational Acceleration g	9.8 m/s^2	9.8 m/s^2
Thermal Expansion Coefficient β	0.0029 K^{-1}	0.0029 K^{-1}
Air Density ρ_{air}	1.02 kg/m^3	0.43 kg/m^3
Dynamic Viscosity μ_{air}	1.85e-5 Ns/m^2	1.85e-5 Ns/m^2
Kinematic Viscosity ν_{air}	1.82e-5 m^2/s	4.3e-5 m^2/s
Specific Heat $C_{\rho,air}$	1009 J/kg·K	1009 J/kg·K

C. High-Altitude Impact

In high-altitude applications, the harsh environment causes deterioration of convective $R_{\text{th,conv}}$ due to the decreased air density. Table I lists the parameters of air at both sea level and 7620 m (25 000 ft) in 75 °C ambient. Fig. 3 further shows the comparisons of calculated $R_{\text{th,conv}}$ at different altitudes with different natural convective areas A_{conv}. Due to air's lower ρ and higher ν, Gr and Pr are influenced, and $R_{\text{th,conv}}$ at 7620 m

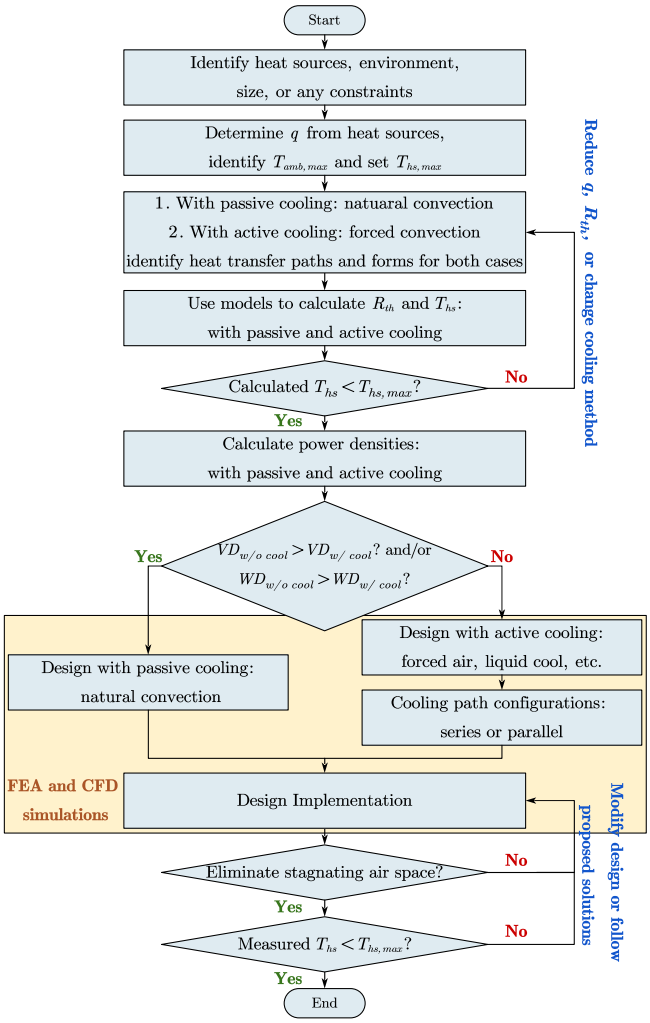

Fig. 4. Proposed design process of thermal management.

becomes higher than that at sea level. Fig. 3 also suggests that the thermal path is mainly determined by $R_{\text{th,conv,top}}$ and $R_{\text{th,conv,bot}}$ in which $R_{\text{th,conv,ver}}$ can be neglected.

D. Design Process of Thermal Management

Fig. 4 presents a design process of thermal management. First, the heat sources and ambient environment of the inverter should be identified. Once q from the heat source is obtained, a decision must be made to use either natural convection (with passive cooling) or forced convection (with active cooling) based on the volume density (VD) and weight density (WD) of the two cases. Based on the power dissipation of the object, a cooling method with sufficient cooling capacity can be preliminarily selected. T_{hs} can be estimated by using models presented in Figs. 1 and 2. If q cannot be further decreased, the loop R_{th} should be minimized by modifying geometry parameters or adopting more advanced cooling. Once T_{hs} meets the targeted temperature $T_{\text{hs,max}}$, the VD and WD of both cases can be calculated and compared to make a final decision based on the application's requirement. In addition, if the cooling method is used to cool multiple heat sources, the cooling path can be arranged in either series or parallel

TABLE II
SPECIFICATIONS OF 3-L T-TYPE INVERTER

Parameters	Value
Power Rating P_o	200 kW
Continuous Output Current i_o	300 Arms
DC Voltage V_{DC}	500-1000 V
Power Factor φ	0.91
Modulation Index MI	0.87
Peak Efficiency η	$\geq$ 99 %
Ambient Temperature T_{amb}	75 °C
Operating Altitude	$\leq$ 7,620 m (25,000 ft)
EMI Standard	DO-160

configurations. The design stage should also consider electrical performances, and the process can be optimized utilizing finite element analysis (FEA) or computational fluid dynamics (CFD) simulations. It is crucial to identify any stagnating air space in the designed structure. As power inverters become more compact, the trapping heat in stagnating air space can cause hotspots in surrounding components. Section V presents the impact of stagnating air space and proposed solutions. To demonstrate the design process, thermal designs and mitigation strategies are presented for a 200-kW high-density 3-L T-type SiC-based propulsion inverter.

III. DEMONSTRATED 3-L T-TYPE INVERTER

A. Demonstrated 3-L T-Type Inverter

Table II summarizes the specifications of the demonstrated 3-L T-type inverter, and Fig. 5 shows the single-phase circuit and overview of the designed inverter assembly. The inverter is required to operate to a thermal steady state at the full-load condition at high altitude, i.e., V_{dc} range of 500–1000 V and i_o of 300 Arms at 7620 m. In accordance with the design process illustrated in Fig. 4, the heat sources in the demonstrated inverter can be identified as busbars, power devices, dc-link capacitors, and dc and ac EMI filters. The inverter adopts PCB-busbar technology for laminated busbar to control the e-field for insulation. The losses in the PCB busbars are generated when conducting currents such as dc current I_{dc}, capacitor current i_C, device current i_S, and output current i_o between nodes. For a worst case scenario in thermal design, the maximum current values should be used in calculations. The copper trace resistance R_{PCB} can be easily calculated using available standards [74], [75]. The power devices in the inverter contribute to dissipated loss mainly from switching and conduction losses. The losses incurred in different switching positions depend on the adopted PWM scheme, switching status, and operating conditions [76]. In this work, the inverter employs the conventional modulation of 3-L SPWM. Figs. 6 and 7 illustrate the normalized switching loss and current distributions in different switching positions over one line cycle, obtained from the circuit-level simulations. The results show that the generated losses are significantly affected by the power factor φ and the modulation index (MI). In particular, switching position S_1/S_4 generates more switching loss at high φ, and conducting currents between S_1/S_4 and S_2/S_3 become more balanced at high MI.

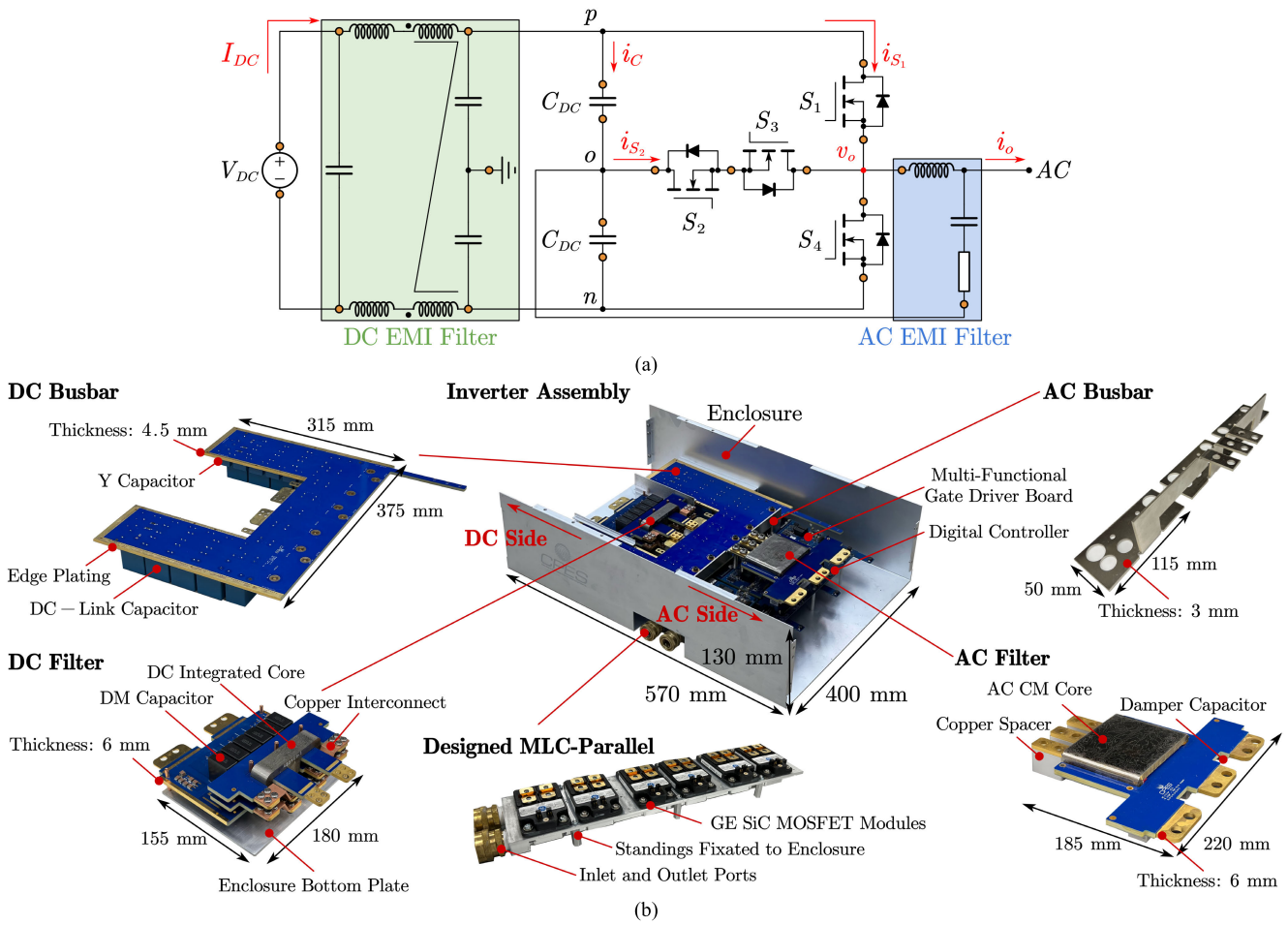

Fig. 5. (a) Single-phase circuit and (b) designed assembly of the demonstrated 200-kW 3-L T-type propulsion inverter with EMI filters. Critical conducting currents between connecting nodes of components are highlighted in the circuit diagram. For the convenience of displaying the inverter, power cables, some connectors, and spacers, as well as the top and side plates of the enclosure, are removed.

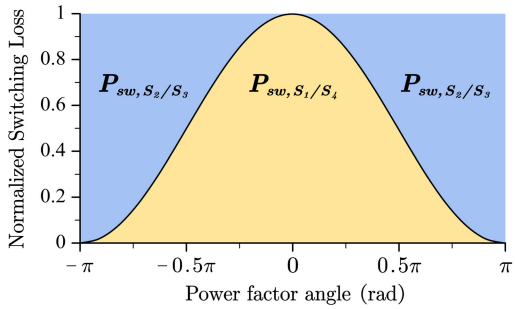

Fig. 6. Switching loss distribution in S_1/S_4 and S_2/S_3 by using 3-L SPWM schemes.

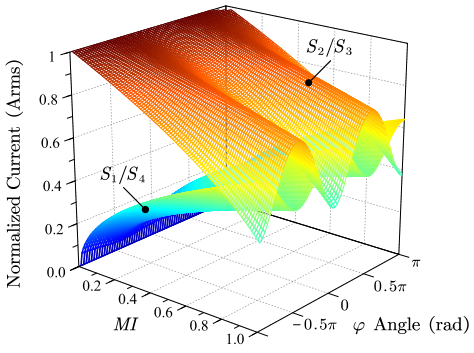

Fig. 7. RMS currents distribution in S_1/S_4 and S_2/S_3.

The dc-link capacitor bank is designed to handle the switching current and limit the voltage ripple across the capacitor bank under all operating conditions. The capacitor loss P_C is generated when capacitor current i_C with switching ripples flows through the capacitor bank [77]. The losses of both dc and ac filters are mainly determined by conduction losses when currents conduct in the filter windings. The maximum currents in dc and ac filter windings are $I_{\rm dc}$ and i_o, respectively. In addition, the total core loss can be estimated by the improved Generalized Steinmetz Equation (iGSE) [78].

Table III summarizes all critical currents and dissipated losses in the inverter based on specifications in Table II. By conducting systematic optimization [79], a total of six 1200-V SiC MOSFET modules from GE shown in Fig. 8 are selected as power devices. The values in Table III will be used for temperature estimation and thermal design.

B. Thermal Mitigation Techniques and Design Workflow

The initial geometry for a thermal design is usually determined by the electrical components. The next step is to identify

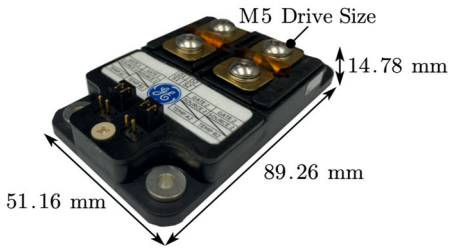

Fig. 8. Selected SiC MOSFET module.

TABLE III
LOSS DISSIPATION IN DEMONSTRATED 3-L T-TYPE INVERTER

Parameters	Value
DC Current I_{DC}	285 A
Capacitor Current i_C	159 Arms
Power Device Current of S_1/S_4	162 Arms
Power Device Current of S_2/S_3	193 Arms
DC-Link Capacitor Unit	TDK B3277 1200V Series
Power Devices of S_1/S_4 and S_2/S_3	GE Dual SiC MOSFET Module
Dissipated Loss of S_1 & S_4	198 W
Dissipated Loss of S_2 & S_3	98 W
DC Filters Current	Same as I_{DC} = 285 A
DC Filters Core Loss	2.4 W
AC Filters Current	Same as i_o = 300 Arms
AC Filters Core Loss	0.5 W

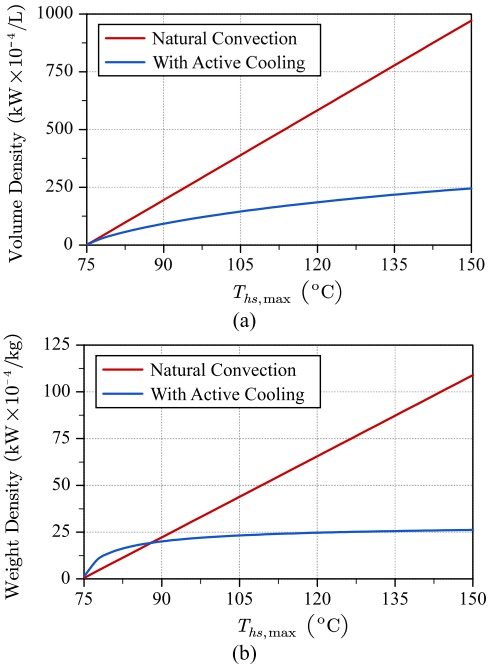

Fig. 9. Comparisons of (a) VD and (b) WD for PCB busbar under conditions of passive cooling and active cooling.

thermal paths and forms, with the aim of reducing thermal resistance R_{th} along the heat transfer path. In a system with passive cooling, such as the one shown in Fig. 1, heat is mainly transferred through $R_{th,cond}$ and $R_{th,conv}$, while $R_{th,rad}$ becomes more significant only in a vacuum environment. To mitigate $R_{th,cond}$ in (1), the thickness L_{cond} can be reduced, or k_{cond} and A_{cond} can be increased. To reduce $R_{th,conv}$ in (2), h_{conv} and the area A_{conv} can be increased. As presented in (5), natural convection is most intense at the top surface, so it is desirable to place heat sources facing upward to achieve a higher h_{conv}.

Conduction is much more effective than convection for heat transfer efficiency. If heat is difficult to dissipate by natural convection alone, an additional conduction path, such as using TIM to fill the air gap, can help reduce the total loop R_{th}. If the forced cooling technique is adopted, Fig. 2 explains the improvements between different cooling solutions. The forced air-cooling method can significantly increase h_{conv} by improving Nu in (3). Different approaches, such as optimizing fin efficiency for MLC, jet impingement, two-phase cooling, and immersion cooling, seek to improve either h_{conv} or A_{conv} to reduce $R_{th,conv}$. Using a heat spreader like a heat pipe or vapor chamber can further reduce $R_{th,cond}$, $R_{th,spre}$, and $R_{th,conv}$ due to the wick's high spreading performance and the fluid's two-phase transition nature [46]. For the double-side cooling method, the cooling area is basically doubled [60], [61].

To decide whether to adopt passive or active cooling methods for heat sources, power densities should be compared. Taking the PCB busbars as an example, the ambient temperature is set to 75 °C. Since the footprint area of PCB busbars is preliminarily determined by electrical components, the losses from all PCB busbars can be easily calculated with the current values in Table III. When passive cooling is adopted, the generated heat of the PCB busbars is dissipated through natural convection, and T_{hs} can be estimated using the model in Fig. 1. To keep the temperature within $T_{hs,max}$, the heavy copper PCB technology is adopted, and the copper thickness is increased to minimize the electrical resistance.

On the other hand, if active cooling is adopted to cool PCB busbars, T_{hs} can be calculated using the model in Fig. 2. Because of the low heat flux, the forced air-cooling solution is selected to compare the power densities with the case with passive cooling. If $T_{hs,max}$ is set to a lower value, the sizes of the heat sink and required fans are increased to achieve a lower loop R_{th}. The total volume and weight can be estimated based on the documented data from off-the-shelf products.

Fig. 9 shows the comparisons of VD and WD between the two cases. When $T_{hs,max}$ is set to a specific value, the case with passive cooling always has higher VD than the case using forced air cooling. Furthermore, when $T_{hs,max}$ is set to be higher than 87 °C, the case with passive cooling also has higher WD than the case with active cooling. By increasing the copper thickness of busbars, T_{hs} can be kept within $T_{hs,max}$ without mounting bulky heatsink and fans. The workflow can be applied to other heat sources. For power devices with high heat flux, if passive cooling is adopted, the resulting power densities to keep T_{hs} within $T_{hs,max}$ are extremely low. Therefore, active cooling solutions should be adopted to cool power devices.

C. Thermal Design for Localized Heat Sources

Fig. 5(b) depicts the inverter assembly and the various components that are designed for the dc busbar, dc filter, ac filter, and ac busbars. To address the thermal issue of localized heat sources, $T_{hs,max}$ is set to 130 °C for all operating conditions. The designed boards utilize heavy copper

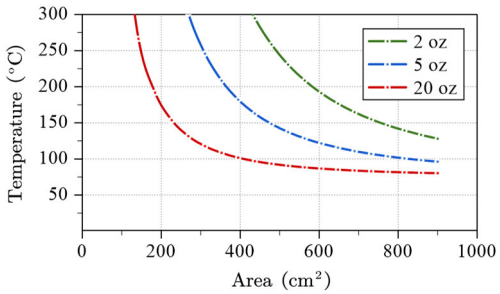

Fig. 10. Estimated temperatures using different copper thicknesses for PCB busbar at an ambient of 75 °C and an altitude of 7620 m.

PCB technology. Fig. 10 illustrates temperature comparisons obtained using different copper thicknesses while conducting a current of 300 A. The results indicated that the 2-oz copper is inadequate to withstand the harsh environment at high altitudes. By using 20-oz copper, the temperature could be lowered to below 130 °C for a footprint area larger than approximately 275 cm^2.

The dc busbar has three main potential layers, namely, p, n, and o potentials that are responsible for conducting high currents. Each potential layer is manufactured with a copper thickness of 0.8 mm to ensure optimal thermal and current density performance. In addition, the edge plating technique is utilized to ensure that the board is in direct contact with the enclosure, providing an additional conduction path. The dc-link capacitors are positioned below the dc busbar and are also in contact with the bottom of the enclosure. As a result, the enclosure served as a large heatsink for the dc busbar and capacitors, and the surface of the PCB is exposed to the top direction, thereby accelerating natural convection based on (5).

The dc EMI filter features a three-turn winding with an integrated DM-CM core structure, as shown in the bottom left of Fig. 5(b). To handle the dc current $I_{\rm dc}$ of 285 A, two layers of 2-mm-thick copper and a current density of 3.4 A/mm^2 are selected for PCB-based windings. The winding turns are connected by copper interconnects, which are firmly fixated by four M5 screws to provide sufficient $A_{\rm cond}$ and reduce the air gap between parts. Moreover, the dc integrated core is positioned naturally on the bottom plate of the enclosure, serving as both a grounding connection and a conduction path for heat dissipation. The ac busbars that conduct i_o of 300 Arms have a copper thickness of 3 mm. They are separated from other PCBs to improve heat dissipation by exposing themselves to the air without FR4 material layers. The ac EMI filter shown in the bottom right of Fig. 5(b) features a single-turn winding structure realized by using heavy copper PCB with two 2-mm-thick copper layers. The ac CM core is designed to have a large contacting area $A_{\rm cond}$ with the PCB. For more detailed design optimization of the dc and ac filters, please refer to [80], [81], [82], and [83].

Fig. 11 depicts customized screws and spacers that are utilized to connect the boards. Copper is used as the material for these customized parts due to its higher $k_{\rm cond}$ compared to the steel alloy of off-the-shelf parts. The copper parts provide lower conducting resistance and reduce $R_{\rm th,cond}$ by improving $k_{\rm cond}$ and $A_{\rm cond}$ from a wider screw head and body

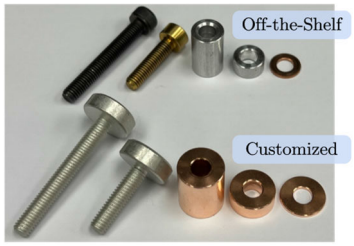

Fig. 11. Off-the-shelf products and customized copper parts.

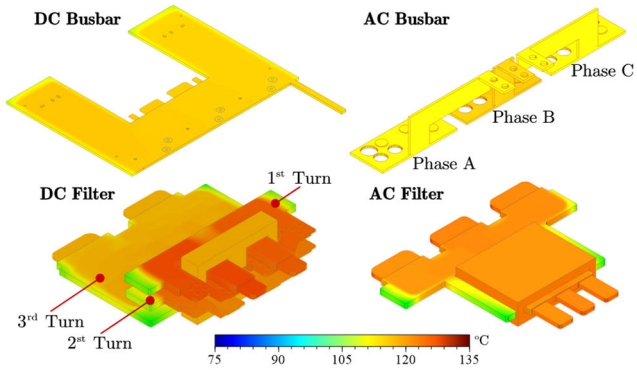

Fig. 12. ANSYS thermal FEA simulation results for localized heat sources.

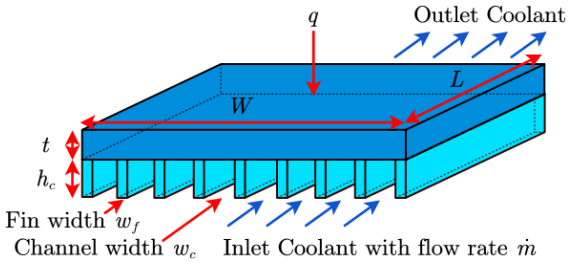

Fig. 13. Physical structure of MLC.

TABLE IV
LIQUID-COOLING CONDITIONS FOR POWER DEVICES

Parameters	Value
Modules Footprint Area (each) A_M	40.8 cm^2
Desired Junction Temperature $T_{j,max}$	≤ 150 °C
Liquid Coolant	EGW 50/50
Coolant Inlet Temperature T_{inlet}	75 °C
Flow Rate $\dot{m}$	0.05 kg/s - 0.25 kg/s
Maximum Allowable Pressure Drop ΔP_{max}	0.4 bar

radius. Fig. 12 shows the FEA simulations that are performed to validate the thermal designs when boards are conducting currents at an ambient of 75 °C and an altitude of 7620 m. All boards are well controlled below 130 °C by following the design process.

IV. COOLING DESIGN FOR POWER DEVICES

In high-altitude environments, the reduced air density makes it difficult to cool power devices with high heat flux using natural convection or conventional air-cooling methods. To maintain a safe junction temperature T_j within $T_{j,\max}$, an aluminum-based liquid cooling MLC is selected due to its low weight, low cost, and high cooling capability.

A. Design and Optimization of Liquid-Cooling MLC

The MLC is designed based on the highest loss of 198 W from each switching position with an additional thermal margin. The cooling conditions are listed in Table IV. By using the derived model in Fig. 2, the thermal requirement of the MLC can be derived. Fig. 13 shows the physical structure of the MLC. The concept is to increase A_{conv} by fabricating microlevel fins on the fin plate to reduce overall $R_{\text{th,conv}}$ [22]. Using MLC, L_c and increased A_{conv} can be expressed as

$$L_c = \frac{4 \cdot h_c \cdot w_c}{2(h_c + w_c)} \tag{15}$$

$$A_{\text{conv}} = N \cdot (L \cdot w_c + 2 \cdot L \cdot h_c \cdot \eta_{\text{fin}}) \tag{16}$$

where N is the number of fins and η_{fin} is the fin's efficiency [84]. Nu can be written by correlation studied in [85]

$$Nu = 0.00805 \cdot Re^{0.8} \cdot Pr^{0.33} \tag{17}$$

where Re is the Reynolds number that describes the fluid characteristics. In addition to the thermal performance, the pressure drop ΔP between the inlet and outlet coolants is also important since it determines the required external pumping power P_{pump}

$$P_{\text{pump}} = \frac{m}{\rho} \cdot \Delta P \tag{18}$$

$$\Delta P = f \frac{L}{L_c} \frac{\rho \cdot {u_{\text{cha}}}^2}{2} + 1.5 \frac{\rho \cdot {u_{\text{cha}}}^2}{2} \tag{19}$$

$$u_{\text{cha}} = \frac{\dot{m}}{N \cdot h_c \cdot w_c \cdot \rho} \tag{20}$$

where f is the Fanning friction factor [84] and u_{cha} is the coolant velocity in a single channel. The MLC with lower ΔP helps in reducing the weight of the external pump since the size of the pump is usually positively related to its rating power. The design process of the MLC is illustrated in Fig. 14. The idea is to shrink the fin height h_c to reduce the weight of the MLC while still meeting all requirements [30]. Once the initial conditions are identified, the performance and weight can be calculated depending on geometry parameters.

B. Comparisons of Cooling Path Configurations

To effectively cool multiple power devices using MLC, it is necessary to compare the performance of different cooling path configurations, such as series and parallel configurations, following the design process [31]. Thus, the MLC optimization is separately conducted for both configurations, and their performances are further compared through CFD simulations. The designed MLCs for both configurations, namely, MLC-Series and MLC-Parallel, are shown in Fig. 15, with loose part samples illustrating the internal fin structure. Fig. 15(a) and (b) shows the base plates of both designs, with the power modules on MLC-Series cooled by the total amount of mass flow rate $\dot{m}$, while $\dot{m}$ in MLC-Parallel is separated into six paralleled branches. The effect of design optimization is revealed in Fig. 15(c) and (d). Here, minimizing h_c eliminates additional volume on the back side of the MLCs. The MLC-Series and MLC-Parallel weigh 671 and 810 g, respectively. Fig. 15(e) and (f) compares the corresponding fin plates of

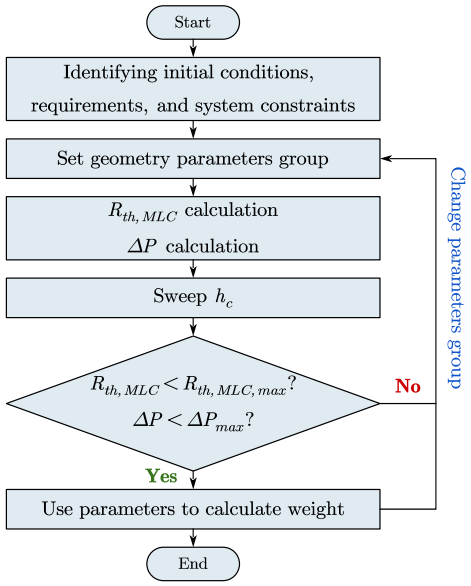

Fig. 14. Flowchart of MLC optimization to achieve minimum weight.

both versions, with the MLC-Series having fewer fins than MLC-Parallel, due to the characteristic of large ΔP caused by a long distance L in (19). Installing more fins would increase u_{cha} due to a narrower channel and eventually exceed ΔP_{max}. Conversely, the MLC-Parallel has a larger ΔP margin, allowing more fins to be manufactured.

To compare the thermal performances, the CFD simulation results using Star-CCM+ are shown in Fig. 15(g) and (h). Each module is assigned to dissipate 300 W (total 1800 W), while $T_{\text{cool,in}}$ and $\dot{m}$ are set to be 75 °C and 0.25 kg/s, respectively. The modules are not included in the CFD simulations to show the surface temperature of the MLCs. The results show that the highest surface temperature of MLC-Series is 87 °C, which is lower than 89 °C of MLC-Parallel, but only at the top right corner where no coolant path is present. If only focusing on the fin plate locations where the modules are mounted, the MLC-Parallel has a temperature of only 78 °C, which is 3 °C lower than the 81 °C of the MLC-Series, indicating that the former has a better dissipation efficiency for power modules than the latter. Fig. 15(i) and (j) further shows that ΔP of the MLC-Parallel is several times lower than that of the MLC-Series, implying that using an MLC-Parallel would result in a lighter external pump. Although MLC-Parallel is slightly heavier than MLC-Series, when considering a footprint area of 360 cm^2, it is at least 40% lighter than most off-the-shelf cold plates on the market. Therefore, the MLC-Parallel is chosen as the final design due to its better efficiency and ΔP performances.

V. Thermal Issue of Stagnating Air Space

While the individually designed parts meet the thermal requirements, the high-density inverter is still prone to stagnating air spaces after assembly. As shown in the design process in Fig. 4, the next step is to avoid or mitigate the impact caused by stagnating air space. It is most desirable to eliminate it at the beginning of the design stage and, however, is also hard to anticipate the impact at the time.

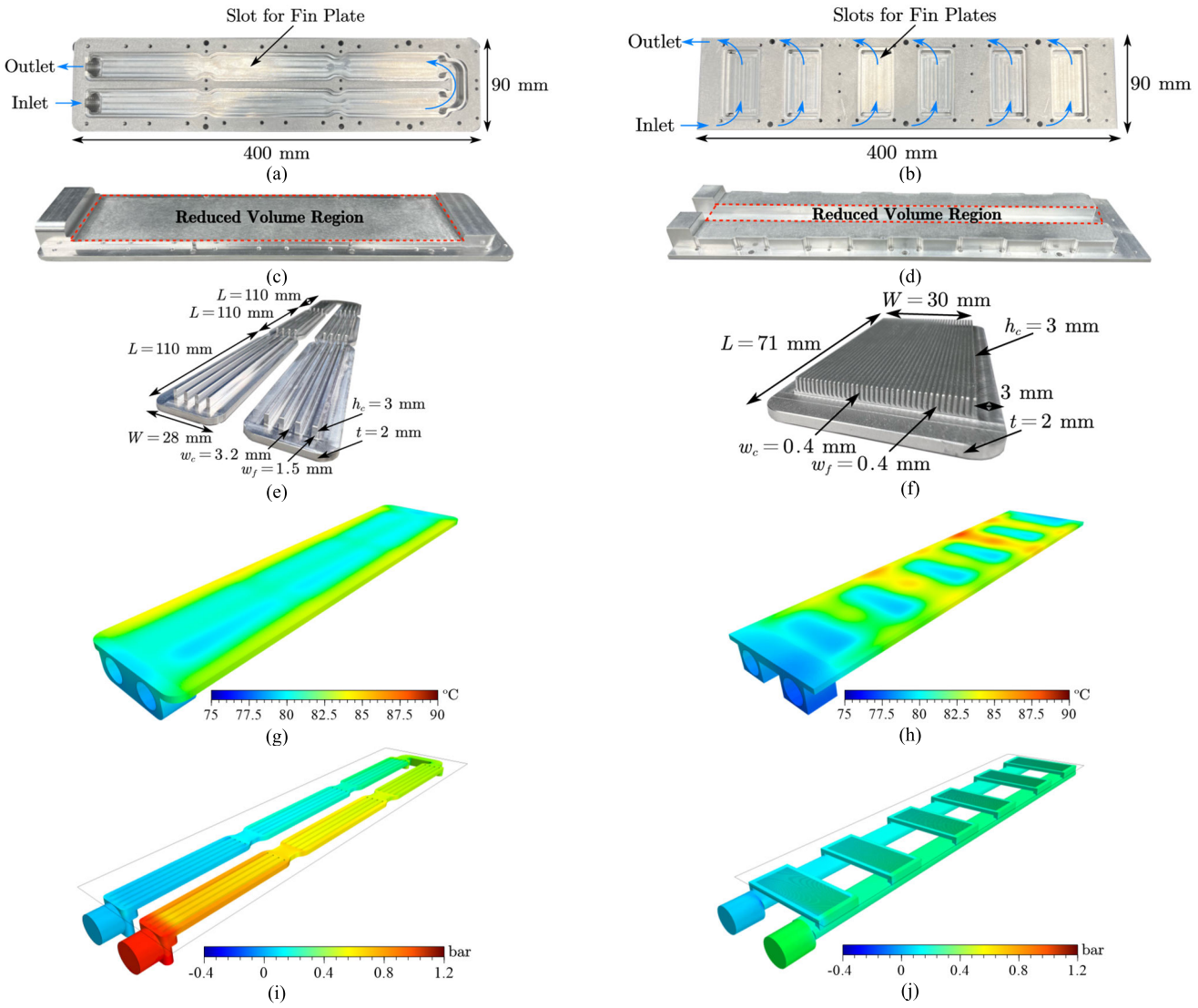

Fig. 15. For the MLC-Series: (a) base plate, (c) back side, (e) fin plate, (g) thermal simulation, and (i) pressure-drop simulation. For the MLC-Parallel: (b) base plate, (d) back side, (f) fin plate, (h) thermal simulation, and (j) pressure-drop simulation. The CFD simulation results are obtained from Star-CCM+.

A. Thermal Impact of the Stagnating Air Space

The negative impact of stagnating air space on thermal performance is demonstrated by the inverter structure in Fig. 5(b). The side view of the board configuration is shown in Fig. 16(a). To optimize the commutation loops, the p, o, and n potential layers are embedded in the gate driver board. These layers, along with decoupling MLCCs, work together with the ac busbars to form loops [86], [87]. However, as indicated by the red dashed box, a stagnating air space is formed, which is trapped by the dc busbar, dc-link capacitors, gate driver boards, and ac busbars. Furthermore, both sides of the air tunnel are blocked by the enclosure. Fig. 16(b) highlights the stagnating air space, and the corresponding CFD simulation result is shown in Fig. 16(c) with thermal conditions listed in Table V. Heat is generated when currents conduct through MLCC vias on gate driver boards and ac busbars, which leads to an undesirable high temperature of around 180 °C on the left-hand side of the driver boards. Although the ac busbars on the right are exposed to ambient air, the temperature still reaches almost 150 °C. It is clear that the stagnating air space has a detrimental effect on thermal performance and is created due to the combination of optimal electric performance and high-density nature.

TABLE V
CONDITIONS OF STAGNATING AIR SPACE IN SIMULATION

Parameters	Value
Ambient Temperature	75 °C
Altitude	7,620 m
Loss from MLCC Vias on each Gate Driver Board	26.5 W
Loss from each AC Busbar	2.3 W
Loss from Screws (per phase)	1.2 W
Loss from Spacers (per phase)	0.5 W

B. Proposed Solutions for the Stagnating Air Space

To mitigate the impact of stagnating air space in a sealed enclosure, several solutions are proposed as follows.

1) *Modify or Redesign the Inverter Structure:* This solution involves eliminating existing stagnating air space or

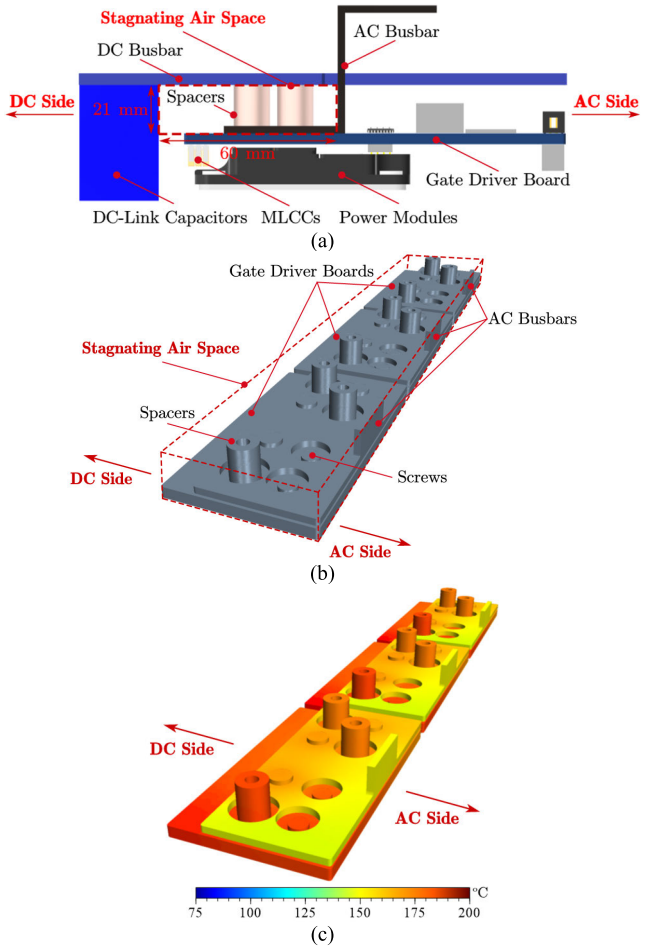

Fig. 16. (a) Side view of board structure, (b) highlighted stagnating air space, and (c) thermal impact obtained from Star-CCM+ simulation.

hotspots by modifying or redesigning the inverter structure. While suitable for early stage design processes, achieving the original optimal electrical performance may not be possible, and the redesign process can be time-consuming and costly.

2) *Introduce Additional Cooling Methods:* This solution involves installing additional heatsinks or cold plates to cool the high-temperature regions. It is a cost-effective and time-efficient solution that allows for maintaining the original optimal electrical performance. However, it may increase the weight of the inverter due to additional parts, and the required power of fans, external heat exchangers, or pumps may further increase external system weight.
3) *Introduce Circulating Air to Harmonize the Temperature Distribution in Sealed Enclosure:* This solution involves introducing circulating air to eliminate the stagnating air spaces by using an internal cooling air duct (AD). The circulating air stream can be created by using an internal fan or from external air sources. It requires minimal cost and time, and original optimal electrical performance can also be maintained. Moreover, the fan and AD add little weight to the inverter system. However, fan-generated acoustic noise and AD's optimal airflow require additional design efforts.

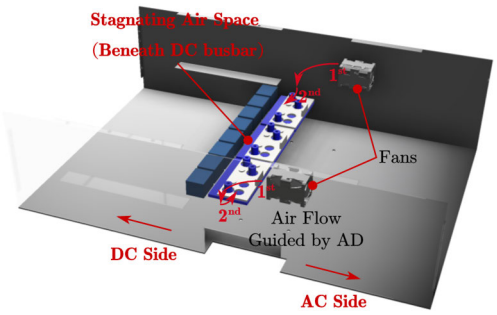

Fig. 17. Proposed solution for eliminating stagnating air space to prevent enlarging the enclosure.

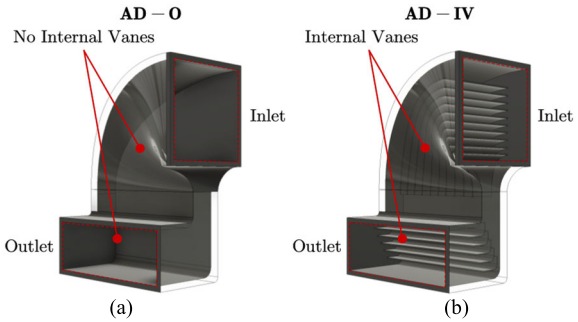

Fig. 18. (a) AD-O and (b) improved AD-IV with internal guided vanes to reduce pressure drop caused by sharp bend turns.

The most appropriate solution for eliminating stagnating air space depends on the specifics of each case. In this study, the method of introducing circulating air by utilizing an internal fan and cooling AD is chosen due to its low cost, short design time, and ability to maintain optimal electrical performance with minimal drawbacks such as increased noise and weight.

C. Location of Fan and AD

Fans provide blowing air, while the AD aims to guide the cooling flow to the hotspots. When space is not a constraint, the conventional rectangular AD (AD-REC) is a good option due to its simple and designless structure. However, in most cases, the remaining space inside the sealed enclosure is limited, and the AD-REC cannot fit. To overcome this dilemma, an alternative solution is proposed in Fig. 17, which highlights the stagnating air space with fans installed on both internal sides of the enclosure. This solution requires designed AD to guide the air through two 90° turns and provide consistent airflow to the stagnating air space. Fig. 18(a) shows the conceptual original AD (AD-O) without airflow optimization. The AD-O serves as a design benchmark and is optimized through the next two steps.

D. Internal Airflow Optimization: Vanes Design

The purpose of the fan is to provide the necessary power to overcome the head loss h_L experienced by the air as it flows through the path including AD. The relationship can be simplified from the extended Bernoulli equation and expressed as

$$h_L = \frac{p_{f,o} - p_{f,i}}{\gamma} = \frac{\Delta P}{\gamma} \tag{21}$$

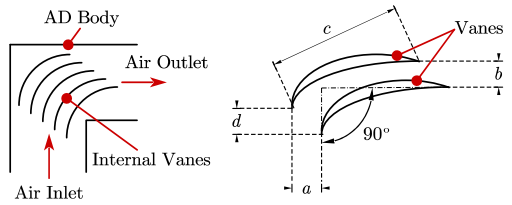

Fig. 19. Guided vanes structure and geometry parameters.

where γ is the specific weight of the fluid, and $p_{f,o}$ and $p_{f,i}$ are the pressure of the outlet and inlet of the fan, respectively. Equation (21) is valid by assuming that the inlet and outlet ports of the fan have the same flow velocity and height level. It also suggests that the pressure drop ΔP is positively related to h_L. The required fan power P_{fan} can be expressed as a function of AD's cross section area $A_{\text{AD},o}$ and velocity $V_{\text{AD},o}$

$$P_{\text{fan}} = A_{\text{AD, o}} \cdot V_{\text{AD, o}} \cdot \Delta P. \tag{22}$$

From (22), if P_{fan} and $A_{\text{AD},o}$ is fixed, an AD with a smaller ΔP(or h_L) can result in higher $V_{\text{AD},o}$. Since h_{conv} is positively related to the flow velocity, an AD with higher $V_{\text{AD},o}$ provides better cooling. By using AD-O in Fig. 18(a), the calculated h_L is around 2.2 [84].

Fig. 18(b) shows the modified AD with optimized internal vanes (AD-IV) to optimize internal airflow. The AD-IV is proposed to reduce h_L for better cooling performance. Internal vanes are installed inside the AD-IV at the locations of two sharp turns. The vane structure is shown in Fig. 19, and the geometry parameters are defined as

$$\alpha = \frac{b}{a} \tag{23}$$

$$\beta = \frac{d}{c}. \tag{24}$$

The comprehensive analysis of vane parameters is studied in [88] and [89]. In this work, α and β are selected as 1 and 0.25, respectively. With the aid of the internal guided vanes, the calculated h_L of AD-IV is around 0.4, which is 5.5 times lower than 2.2 of AD-O.

The impact of internal airflow optimization can be observed from CFD simulations, as shown in Fig. 20(a) and (b), where airflow comparisons are presented at the outlet ports of AD-O and AD-IV, respectively. Line probes are placed to measure airflow velocity along horizontal distances. Using the same fan and having the same outlet area $A_{\text{AD},o}$, it is evident that the AD-IV has much more evenly distributed airflow at the outlet port than the AD-O. The outlet air velocity of AD-O is extremely uneven and accumulates at the bottom of the duct. In contrast, the airflow for the AD-IV, as shown in Fig. 20(b), presents a much better distribution as the air velocity is evenly distributed around 12.5 m/s. The AD-IV efficiently guides the airflow from fan to hotspots even with sharp turns. Furthermore, the cooling performances of AD-O and AD-IV are compared in Fig. 21, using the same conditions in Table V. Both top and side views are shown for airflow and thermal comparisons. Compared with the original case in Fig. 16(c), using AD-O improves the highest temperature from the original 180 °C to 145 °C. However, the design is not satisfactory because the blowing air is unevenly distributed, and consequently, the airflow is unable to cover all hotspots on the gate driver boards. Moreover, the middle phase gate driver board experiences a 10 °C higher temperature than the other two phases. On the contrary, using AD-IV not only reduces the highest temperature to 130 °C but also results in much better temperature distribution among the three phases. Since AD-IV has a lower h_L than AD-O, a higher average V_{AD} at the outlet of AD-IV can be expected, which aids the convective heat transfer efficiency.

E. External Airflow Optimization: Air Blocks Design

The thermal robustness can be further enhanced by optimizing external airflow. In Fig. 21(b), although AD-IV successfully addresses the issue of stagnating air space, some air leaks through certain areas and goes unused. This results in reduced cooling efficiency. To mitigate this issue, an air block is added to the AD-IV, namely, AD-IVB, as shown in Fig. 22(a).

Comparing the performance in Fig. 22(b) with the case using AD-IV in Fig. 21(b), the airflow in Fig. 22(b) penetrates the stagnating air space more efficiently with minimum leaking air. The highest temperature is further reduced to approximately 125 °C. The final designed AD-IVB is 3-D printed using resin, as shown in Fig. 23. Each AD-IVB has a volume of 45 cm^3 and weighs 59 g. The weight is increased to 179 g if the fan and screws are included. The printed AD-IVB can be even lighter by using other materials. The designed AD-IVB proves to be a suitable solution for cases that have limited space to eliminate the stagnating air space. In this way, the optimal electrical performance and inverter structure can remain unchanged.

VI. Experimental Validations

A. System Setup and Full-Power Pump-Back Tests

To conduct the thermal test at full power, two inverters are assembled and arranged in a pump-back configuration, as shown in Fig. 24(a). Both Inverter 1 and Inverter 2 have identical designs. The enclosure for Inverter 1 is opened to the ambient environment to allow for easy monitoring of all hotspots' temperatures, while Inverter 2 is sealed to validate the final thermal design. The edges are sealed with Kapton tape, which creates a worst case scenario due to its low thermal conductivity. Considering safety for thermal tests, all power cables, inverters, and components are arranged carefully to prevent contact with each other. Fig. 24(b) provides a closer view of Inverter 1. The dc busbar is disconnected to reveal the stagnating air space beneath it. Table VI details the testing parameters for the full-power thermal test, while the tested full-power waveforms are presented in Fig. 25. All thermal tests last at least 20 min with V_{dc} around 700 V and i_o of 300 Arms to reach a thermal steady state.

B. Validation of Designed MLC

To evaluate the performance of the MLCs, power resistors of similar size to the power modules are used in preliminary tests. The fin and base plates of the tested MLCs are soldered

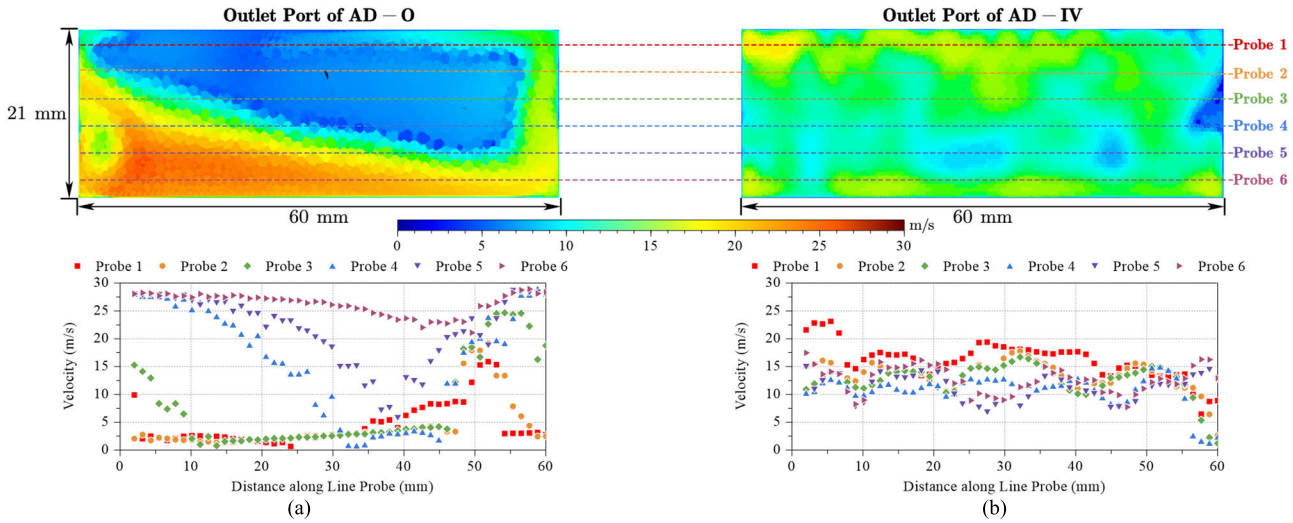

Fig. 20. Comparison of airflow distribution at the outlet port of (a) AD-O and (b) AD-IV.

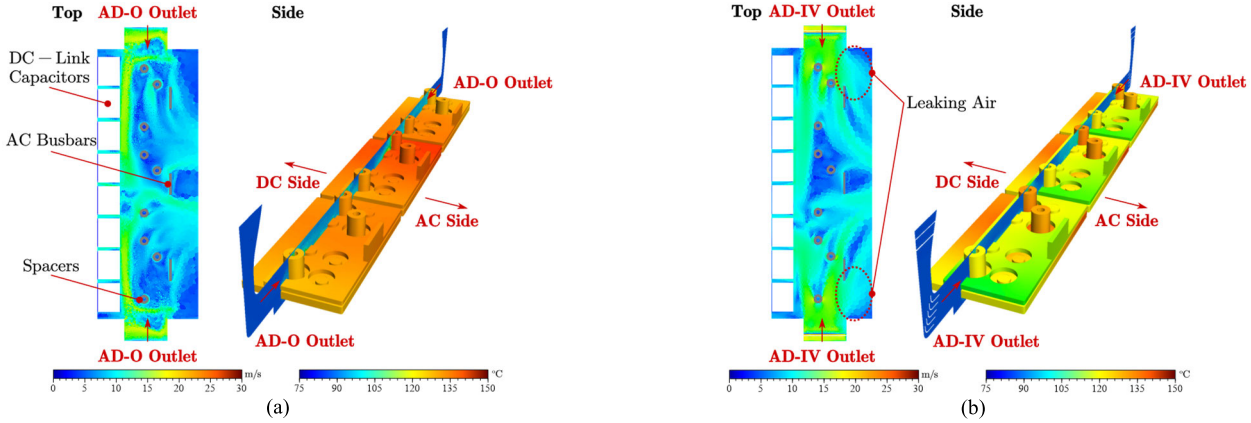

Fig. 21. Comparisons of airflow and cooling performance by using (a) AD-O and (b) AD-IV in CFD simulations.

TABLE VI
PARAMETERS FOR FULL-POWER PUMP-BACK TEST

Parameters	Value
Peak AC Output Current $I_{o,pk}$	424 A
DC Voltage V_{DC}	≈ 700 V
DC Current I_{DC}	252 A
Power Factor φ	0.99 for Inverter 1 -0.99 for Inverter 2
Modulation Index	0.8
Dissipated Loss of S_1 & S_4 in Inverter 1	192 W
Dissipated Loss of S_2 & S_3 in Inverter 1	144 W
Room Temperature	25 °C
Coolant	EGW 50/50
Inlet Coolant Temperature $T_{cool,in}$	30 °C
Coolant Flow Rate $\dot{m}$	0.25 kg/s

together by the manufacturer to ensure a leakage-free system. $\dot{m}$ is controlled by the external heat exchanger and chiller, and is monitored by the flowmeter. Figs. 26 and 27 show the comparisons of $R_{\text{th,MLC}}$ and ΔP performances of MLC-Series and MLC-Parallel, respectively. In both Figs. 26 and 27, the CFD simulation results well correspond to the mathematical predictions for both $R_{\text{th,MLC}}$ and ΔP. In Fig. 26(a), compared to the model results, the experimental $R_{\text{th,MLC}}$ has an overall error of less than 30% and is always higher than the results obtained from the mathematical model. The experimental ΔP in Fig. 26(b) is also 0.05 bar higher than the results from both model and CFD simulations. This error may be caused by the reading error from measurement. On the other hand, in Fig. 27(a), the experimental $R_{\text{th,MLC}}$ of MLC-Parallel is always higher than mathematical results with a maximum error of around 28.5%. However, as shown in Fig. 27(b), differences of ΔP are discovered between model and experimental results. The experimental ΔP is larger than both the model and CFD simulations. It is suspected that this difference is caused by the fabrication defects of the fin plate.

Fig. 28 shows the loose part sample of the fin plate of MLC-Parallel. The deformation of fins and small particles on the fin plate may block the channel and result in higher ΔP. It is found that the optimized performance of MLC-Parallel requires the effort of fine manufacturing. Since the channels of MLC-Series are much wider than those of MLC-Parallel, no major defects are observed, so the experimental results match with the model and CFD simulations with small errors. Despite that, the measured maximum ΔP of MLC-Parallel is always lower than 0.37 bar, which is three times lower than that of the MLC-Series. As a result, the MLC-Parallel is a

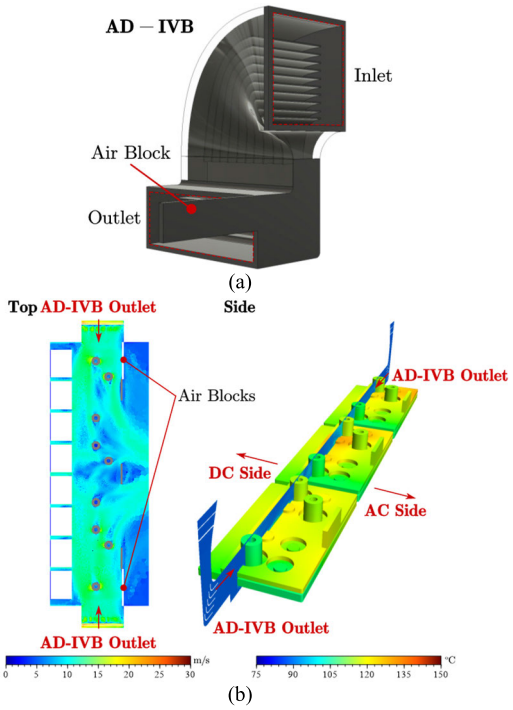

Fig. 22. (a) AD-IVB with air block to improve external airflow and (b) airflow and cooling performances.

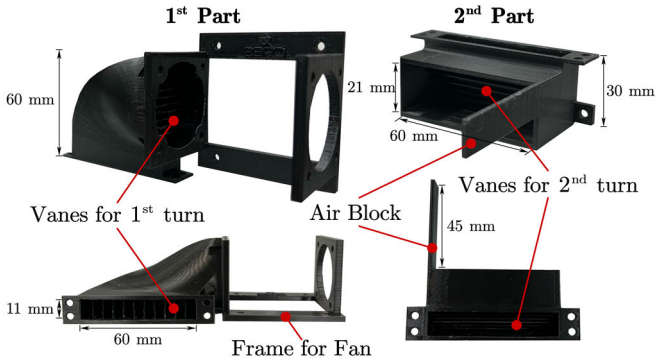

Fig. 23. AD-IVB is 3-D printed into two parts to show the internal vane design.

more attractive design. Since the 30 °C EGW 50/50 has lower thermal conductivity and higher viscosity than the 75 °C one [90], both $R_{\text{th,MLC}}$ and ΔP performances are expected to be better when 75 °C EGW 50/50 is adopted as coolant.

C. Junction Temperature Measurements

The junction temperature T_j is measured by the temperature detector of the power module. The thermal grease TIM with thermal conductivity of 3 W/m·K is applied between modules and MLC-Parallel. All switching positions in Inverter 1 are measured, and the results are summarized in Fig. 29. By using the designed MLC-Parallel, the maximum measured T_j is around 67 °C at full power when $\dot{m}$ is at 0.25 kg/s. Fig. 29 also reveals that the temperature distribution is mainly determined by the loss difference among switching positions in the 3L T-type inverter instead of the configuration of paralleling coolant paths. The small temperature difference among modules may be caused by the fin plate difference. The TIM may also have an impact on temperature distribution if the applied thickness is uneven for different modules.

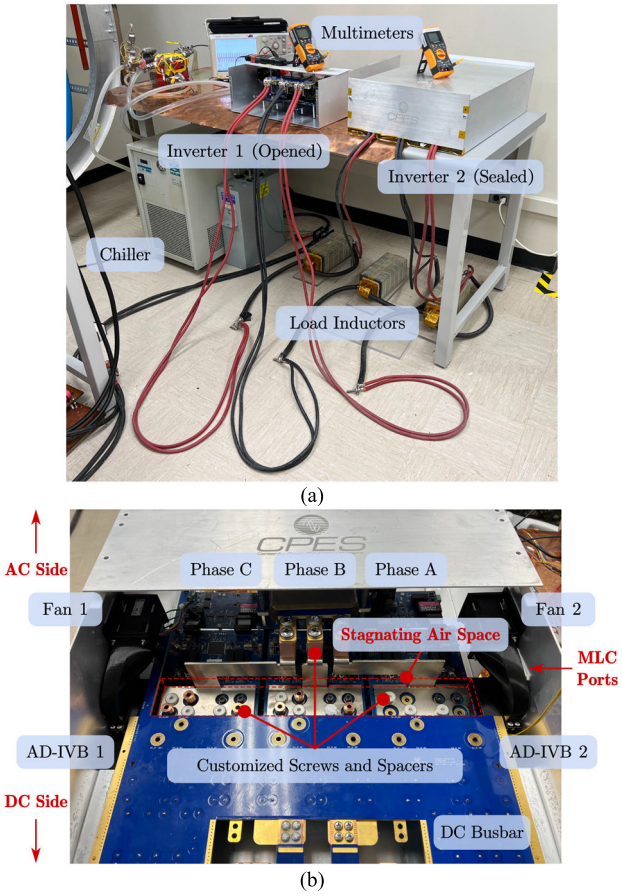

Fig. 24. (a) Pump-back setup and (b) closer view of Inverter 1.

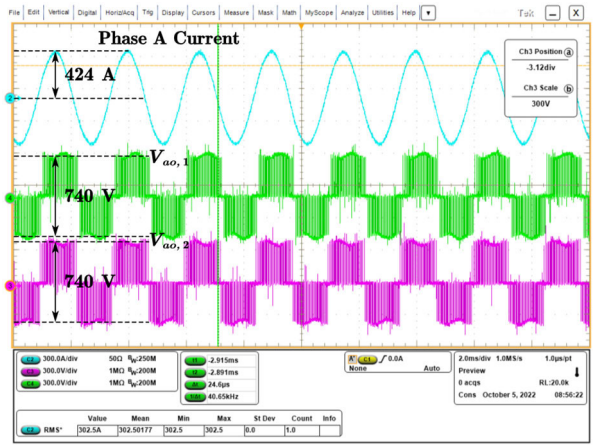

Fig. 25. Waveforms of the continuous full-power pump-back test.

D. Thermal Performance of Localized Heat Sources

Two ADs in Fig. 24(b) are first removed from the inverter to understand the thermal performances of localized heat sources. The temperatures of all heat sources are measured by using K-type thermocouples U1186A with multimeters. A comparison of the two setups is shown in Table VII by using

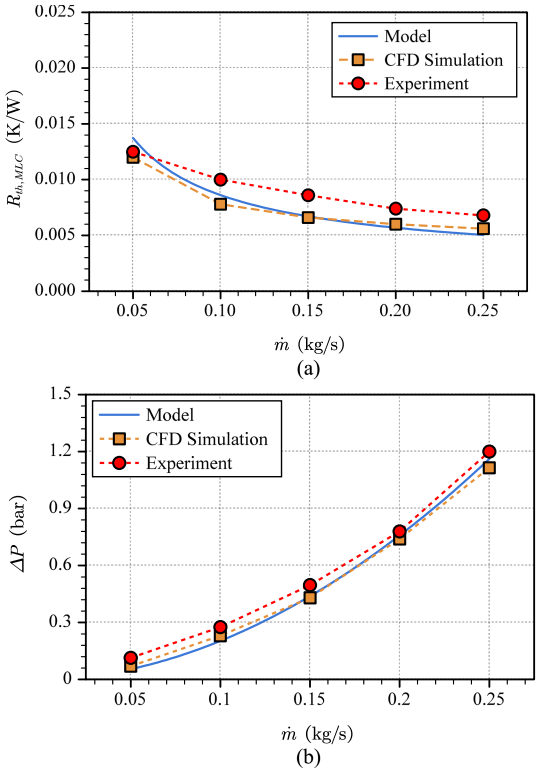

Fig. 26. Result comparisons of (a) $R_{\text{th,MLC}}$ and (b) ΔP of MLC-Series.

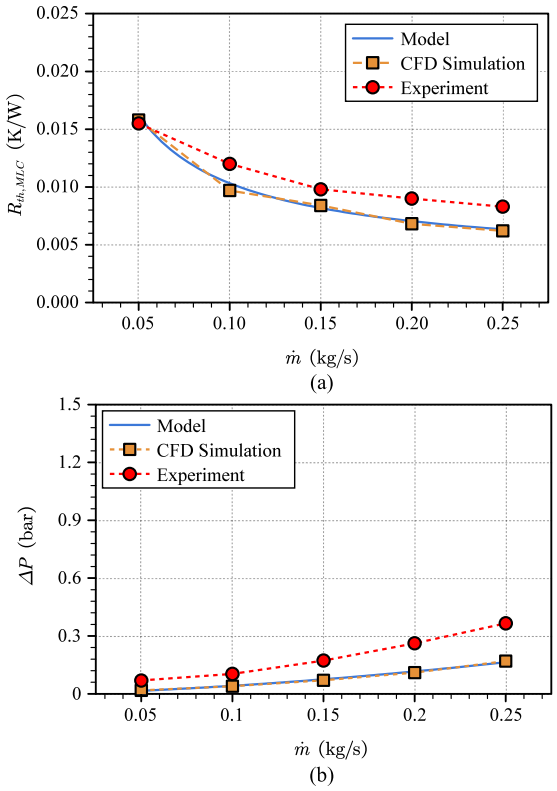

Fig. 27. Result comparisons of (a) $R_{\text{th,MLC}}$ and (b) ΔP of MLC-Parallel.

off-the-shelf and customized parts. The measured temperatures using designed heavy copper PCBs and customized parts are much alleviated compared to the case using off-the-shelf

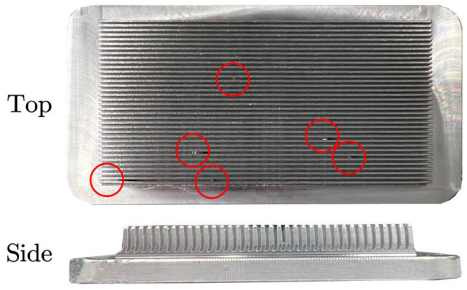

Fig. 28. Fabrication defects of small particles and distorted channels in the loose part sample fin plate of MLC-Parallel.

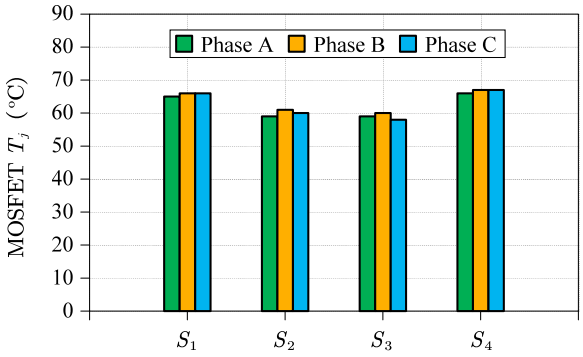

Fig. 29. Measured T_j of power modules in different switching positions when using 30 °C EGW 50/50 as coolant with $\dot{m}$ of 0.25 kg/s.

TABLE VII
MEASURED STEADY-STATE TEMPERATURE OF LOCALIZED HEAT SOURCES AT FULL POWER AFTER 20 MIN

Measured Locations Parts	Off-the-Shelf	Customized
DC Busbar Screws (p, n)	71 °C	61 °C
DC Busbar Screws (o)	84 °C	64 °C
AC Busbar Screws	138 °C	95 °C
MLCC Vias on Gate Driver Board	141 °C	101 °C
DC Filter Core	29 °C	28 °C
DC Filter Winding PCB	54 °C	49 °C
AC Filter Core	45 °C	43 °C
AC Filter Winding PCB	78 °C	63 °C

parts. By replacing parts, the maximum hotspot temperature rise is improved by 34.4%. The highest temperatures can be observed on ac busbar screws and MLCC vias on gate driver boards that are located in the stagnating air space. These locations are highlighted in Fig. 30. It is undesirable to have a temperature of 101 °C on the gate driver boards when tests are conducted at a room temperature of 25 °C. To verify the proposed circulating air AD solution for stagnating air space, the following tests will focus on those hotspot locations shown in Fig. 30.

E. Air Ducts' Validations for Stagnating Air Space

The ADs are later installed in an inverter to improve the hotspot temperatures in the stagnating air space. The fan used in this work is GFB0412ES-E from Delta Electronics. Fig. 31 shows the temperature improvements by using different versions of ADs. By introducing circulating air using AD-O, the temperatures of ac busbar screws and MLCC vias drop

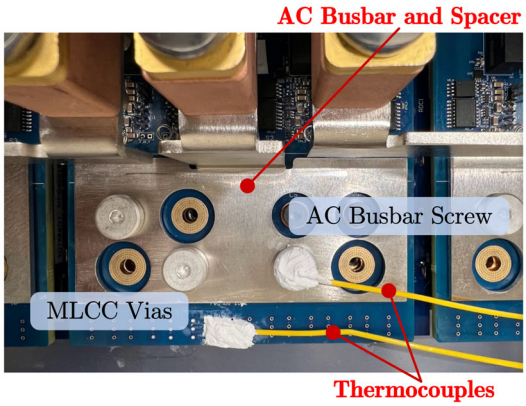

Fig. 30. Two locations of hotspot temperature in stagnating air space.

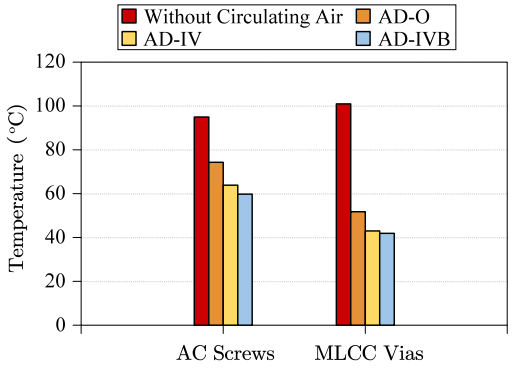

Fig. 31. Measured temperature of hotspots in stagnating air space by using different versions of AD.

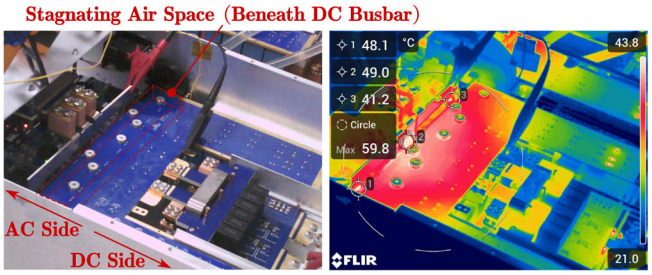

Fig. 32. Thermal images of the full-power thermal test after 20 min.

significantly from 95 °C to 74 °C and 101 °C to a decent 52 °C, respectively. The result in Fig. 31 also suggests the necessity of optimizing the cooling airflow. Due to a smaller h_L, the AD-IV with internal vanes helps decrease temperatures by around 10 °C compared to the case using AD-O. With optimization of both internal and external airflows using AD-IVB, another 5 °C temperature drop is achieved. Fig. 32 shows the phtted thermal images of Inverter 1 using AD-IVB. The heat is observed concentrating in the location of the stagnating air space. The highest temperature of 59.8 °C is only located on the bottom of the middle phase ac busbar. The measured temperature profile validates the thermal designs and proposed solutions for the stagnating air space.

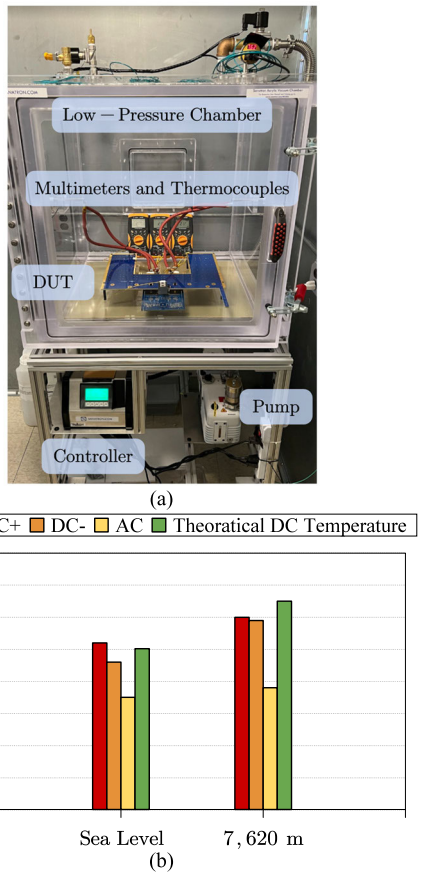

Fig. 33. (a) Pressure chamber test setup and (b) measured temperatures. Due to the limited space, it is unable to place the entire inverter into the chamber.

F. Sealed Enclosure Thermal Test

The thermal design is further tested by using Inverter 2 with a sealed enclosure. Only the temperatures of ac busbar screws are measured since they present the highest temperature in thermal tests and images. Compared to the opened enclosure case, the measured hotspot temperature rise increases approximately 19% in the sealed enclosure from temperature 59.8 °C to 66.4 °C. The enclosure temperature also rises to 31.5 °C since the heat is dissipated to the ambient through the enclosure.

G. High-Altitude Thermal Test

The temperature rise at a high altitude of 7620 m is estimated based on thermal tests conducted in the low-pressure chamber, as shown in Fig. 33(a). The dc busbar, gate driver board, and ac busbar are placed in the low-pressure chamber with thermocouples mounted on them. A dc current of 200 A flows through the dc busbar, and the measured steady temperatures are recorded in Fig. 33(b). When the altitude increases from sea level to 7620 m, the temperature rise increases by around 40%. Since the ac busbar has no current conducting, the temperature rise is not obvious in this test. The error between the theoretical and measured temperature is around 6 °C, which may be caused by airflow difference between the chamber and the real environment [91]. The dynamic viscosity μ and the air density ρ would also

have an impact on natural convection and generate a slightly lower thermal resistance, which results in a lower measured temperature.

To summarize the testing results, the MLCs are first tested, and the accuracy of the mathematical model is validated by both CFD simulations and experimental results. The designed MLC-Parallel is proven to have good $R_{\text{th,MLC}}$ and superior ΔP performances compared to MLC-Series. ΔP of MLC-Parallel is always lower than 0.37 bar within the flow rate range from 0.05 to 0.25 kg/s. The power modules are later mounted on the MLC-Parallel, and the maximum T_j is around 67 °C at full power condition when $\dot{m}$ is at 0.25 kg/s. The temperatures of all localized heat sources are also measured by using thermocouples. By replacing the off-the-shelf mechanical parts with optimized copper parts, the hotspot temperature rise is reduced by 34% for ac screws. Moreover, the temperature rise is further reduced by 54% by introducing circulating air, which is intended to harmonize the temperature distribution within the enclosure. After the enclosure is sealed, a 19% temperature-rise increment is observed from the hotspot temperature. By using the pressure chamber to run thermal tests at the altitude of 7620 m, the temperature rise increases by around 40% compared to that at sea level. Combining all thermal results from the above tests, the maximum hotspot temperature within the sealed enclosure can be estimated as around 130 °C at the ambient temperature of 75 °C and an altitude of 7620 m. Also, the highest temperature only occurs on part of the ac busbar without damaging other electrical components. The experimental results verified the feasibility of the proposed systematic design flow of thermal management.

VII. Conclusion

In this article, a systematic design process of thermal management for a high-density high-power propulsion inverter is presented and demonstrated by a 200-kW 3-L T-type propulsion inverter. Based on the derived thermal models, cooling designs with high density and high efficiency are proposed. In addition, it is found that the stagnating air space created by the high-density structure of the inverter has a detrimental effect on thermal performance and can generate localized hotspots on electrical components. To address the thermal issue, localized AD and a small fan are used to mobilize the stagnated air in a sealed enclosure and harmonize the temperature distribution. By optimizing both internal and external airflows, the designed AD addresses the hotspots effectively without adding extra cooling weight and size. Moreover, the proposed AD solution eliminates the usage of oversized copper parts and terminals. The experimental full-power thermal tests validate the thermal design, showing that the highest temperature of the prototype in a sealed enclosure is around 130 °C at an ambient temperature of 75 °C and an altitude of 7620 m.

Acknowledgment

The authors would like to thank people from the AIRBUS Team who helped arrange the visit, install the motor control units (MCUs), and perform testing.

References

[1] B. Sarlioglu and C. T. Morris, "More electric aircraft: Review, challenges, and opportunities for commercial transport aircraft," *IEEE Trans. Transport. Electrific.*, vol. 1, no. 1, pp. 54–64, Jun. 2015.

[2] S. Yin, K. J. Tseng, R. Simanjorang, Y. Liu, and J. Pou, "A 50-kW high-frequency and high-efficiency SiC voltage source inverter for more electric aircraft," *IEEE Trans. Ind. Electron.*, vol. 64, no. 11, pp. 9124–9134, Nov. 2017.

[3] B. Cougo, H. H. Sathler, R. Riva, V. D. Santos, N. Roux, and B. Sareni, "Characterization of low-inductance SiC module with integrated capacitors for aircraft applications requiring low losses and low EMI issues," *IEEE Trans. Power Electron.*, vol. 36, no. 7, pp. 8230–8242, Jul. 2021.

[4] Z. Wang, Y. Wu, M. H. Mahmud, Z. Zhao, Y. Zhao, and H. A. Mantooth, "Design and validation of a 250-kW all-silicon carbide high-density three-level T-type inverter," *IEEE J. Emerg. Sel. Topics Power Electron.*, vol. 8, no. 1, pp. 578–588, Mar. 2020.

[5] A. K. Morya et al., "Wide bandgap devices in AC electric drives: Opportunities and challenges," *IEEE Trans. Transport. Electrific.*, vol. 5, no. 1, pp. 3–20, Mar. 2019.

[6] J. Ebersberger, M. Hagedorn, M. Lorenz, and A. Mertens, "Potentials and comparison of inverter topologies for future all-electric aircraft propulsion," *IEEE J. Emerg. Sel. Topics Power Electron.*, vol. 10, no. 5, pp. 5264–5279, Oct. 2022.

[7] S. Mocevic et al., "Design of a 10 kV SiC MOSFET-based high-density, high-efficiency, modular medium-voltage power converter," *iEnergy*, vol. 1, no. 1, pp. 100–113, Mar. 2022.

[8] A. L. Moore and L. Shi, "Emerging challenges and materials for thermal management of electronics," *Mater. Today*, vol. 17, no. 4, pp. 163–174, May 2014.

[9] H. Medjahed, P.-E. Vidal, and B. Nogarede, "Thermo-mechanical stress of bonded wires used in high power modules with alternating and direct current modes," *Microelectron. Rel.*, vol. 52, no. 6, pp. 1099–1104, Jun. 2012.

[10] F. Paschen, "Ueber die zum funkenübergang in luft, Wasserstoff und Kohlensäure bei verschiedenen drucken erforderliche potentialdifferenz," *Annalen Physik*, vol. 273, no. 5, pp. 69–96, 1889.

[11] M. Saidi and R. H. Abardeh, "Air pressure dependence of natural-convection heat transfer," in *Proc. World Congr. Eng. (WCE)*, vol. 2. London, U.K., Jun./Jul. 2010, pp. 1–5.

[12] D. Bar-Shalom, "Altitude effects on heat transfer processes in aircraft electronic equipment cooling," M.S. thesis, Massachusetts Inst. Technol., Cambridge, MA, USA, 1988.

[13] E. M. Racine, "Experimental study—High altitude forced convective cooling of electromechanical actuation systems," M.S. thesis, Univ. Dayton Res. Inst., Dayton, OH. USA, 2016.

[14] J. Liu et al., "Design of the Chevrolet Bolt EV propulsion system," *SAE Int. J. Alternative Powertrains*, vol. 5, no. 1, pp. 79–86, Apr. 2016.

[15] J. Reimers, L. Dorn-Gomba, C. Mak, and A. Emadi, "Automotive traction inverters: Current status and future trends," *IEEE Trans. Veh. Technol.*, vol. 68, no. 4, pp. 3337–3350, Apr. 2019.

[16] E. Barbarini and V. Le Troadec, "STMicroelectronics SiC module—Tesla model 3 inverter," Syst. Plus Consulting, Power Semicond., Pays de la Loire, France, Tech. Rep., 2018.

[17] M. Ghanekar, "Vapor cycle system for the F-22 raptor," SAE Tech. Paper 2000-01-2268, 2000.

[18] A. S. van Heerden, D. M. Judt, S. Jafari, C. P. Lawson, T. Nikolaidis, and D. Bosak, "Aircraft thermal management: Practices, technology, system architectures, future challenges, and opportunities," *Prog. Aerosp. Sci.*, vol. 128, Jan. 2022, Art. no. 100767.

[19] P. Wang, P. McCluskey, and A. Bar-Cohen, "Two-phase liquid cooling for thermal management of IGBT power electronic module," *J. Electron. Packag.*, vol. 135, no. 2, Jun. 2013, Art. no. 021001.

[20] I. Aranzabal, I. M. de Alegría, N. Delmonte, P. Cova, and I. Kortabarria, "Comparison of the heat transfer capabilities of conventional single- and two-phase cooling systems for an electric vehicle IGBT power module," *IEEE Trans. Power Electron.*, vol. 34, no. 5, pp. 4185–4194, May 2019.

[21] S. G. Kandlikar and C. N. Hayner, "Liquid cooled cold plates for industrial high-power electronic devices—Thermal design and manufacturing considerations," *Heat Transf. Eng.*, vol. 30, no. 12, pp. 918–930, Oct. 2009.

[22] D. B. Tuckerman and R. F. W. Pease, "High-performance heat sinking for VLSI," *IEEE Electron Device Lett.*, vol. EDL-2, no. 5, pp. 126–129, May 1981.

[23] A. J. Robinson, "A thermal–hydraulic comparison of liquid microchannel and impinging liquid jet array heat sinks for high-power electronics cooling," *IEEE Trans. Compon. Packag. Technol.*, vol. 32, no. 2, pp. 347–357, Jun. 2009.

[24] G. L. Morini, "Single-phase convective heat transfer in microchannels: A review of experimental results," *Int. J. Thermal Sci.*, vol. 43, no. 7, pp. 631–651, Jul. 2004.

[25] P.-S. Lee, S. V. Garimella, and D. Liu, "Investigation of heat transfer in rectangular microchannels," *Int. J. Heat Mass Transf.*, vol. 48, no. 9, pp. 1688–1704, Apr. 2005.

[26] R. W. Knight, D. J. Hall, J. S. Goodling, and R. C. Jaeger, "Heat sink optimization with application to microchannels," *IEEE Trans. Compon., Hybrids, Manuf. Technol.*, vol. 15, no. 5, pp. 832–842, Oct. 1992.

[27] Z.-H. Wang, X.-D. Wang, W.-M. Yan, Y.-Y. Duan, D.-J. Lee, and J.-L. Xu, "Multi-parameters optimization for microchannel heat sink using inverse problem method," *Int. J. Heat Mass Transf.*, vol. 54, nos. 13–14, pp. 2811–2819, Jun. 2011.

[28] N. Hamadneh, W. Khan, and S. Tilahun, "Optimization of microchannel heat sinks using prey-predator algorithm and artificial neural networks," *Machines*, vol. 6, no. 2, p. 26, Jun. 2018.

[29] B. A. Jasperson, Y. Jeon, K. T. Turner, F. E. Pfefferkorn, and W. Qu, "Comparison of micro-pin-fin and microchannel heat sinks considering thermal-hydraulic performance and manufacturability," *IEEE Trans. Compon. Packag. Technol.*, vol. 33, no. 1, pp. 148–160, Mar. 2010.

[30] C.-W. Chang, X. Zhao, R. Phukan, D. Dong, R. Burgos, and P. Arnaud, "Weight-minimizing optimization of microchannel cold plate for SiC-based power inverters in more-electric aircraft," in *Proc. IEEE Energy Convers. Congr. Expo. (ECCE)*, Oct. 2022, pp. 1–8.

[31] H. Chen, Y. Han, G. Tang, and X. Zhang, "Duo-CPU liquid cooling loop configuration: Parallel or series?" in *Proc. 18th IEEE Intersoc. Conf. Thermal Thermomech. Phenomena Electron. Syst. (ITherm)*, May 2019, pp. 70–76.

[32] M.-C. Lu and C.-C. Wang, "Effect of the inlet location on the performance of parallel-channel cold-plate," *IEEE Trans. Compon. Packag. Technol.*, vol. 29, no. 1, pp. 30–38, Mar. 2006.

[33] K. A. Agbim, "Single-phase liquid cooling for thermal management of power electronic devices," M.S. thesis, Georgia Inst. Technol., Atlanta, Georgia, 2017. [Online]. Available: https://repository.gatech.edu/entities/publication/f5cc56d2-c7fa-4df2-a3d3-81daf55d0d7b

[34] Y. Yerasimou, V. Pickert, B. Ji, and X. Song, "Liquid metal magnetohydrodynamic pump for junction temperature control of power modules," *IEEE Trans. Power Electron.*, vol. 33, no. 12, pp. 10583–10593, Dec. 2018.

[35] J. Fan, Y. Zhang, J. Wang, M. S. Chinthavali, and R. K. Moorthy, "Liquid metal based cooling for power electronics systems with inductor integrated magnetohydrodynamic pump (MHD pump)," in *Proc. IEEE 8th Workshop Wide Bandgap Power Devices Appl. (WiPDA)*, Nov. 2021, pp. 310–315.

[36] E. Laloya, Ó. Lucía, H. Sarnago, and J. M. Burdío, "Heat management in power converters: From state of the art to future ultrahigh efficiency systems," *IEEE Trans. Power Electron.*, vol. 31, no. 11, pp. 7896–7908, Nov. 2016.

[37] K. Gould, S. Q. Cai, C. Neft, and A. Bhunia, "Liquid jet impingement cooling of a silicon carbide power conversion module for vehicle applications," *IEEE Trans. Power Electron.*, vol. 30, no. 6, pp. 2975–2984, Jun. 2015, doi: 10.1109/TPEL.2014.2331562.

[38] J. Jörg, S. Taraborrelli, G. Sarriegui, R. W. De Doncker, R. Kneer, and W. Rohlfs, "Direct single impinging jet cooling of a MOSFET power electronic module," *IEEE Trans. Power Electron.*, vol. 33, no. 5, pp. 4224–4237, May 2018.

[39] S. Jones-Jackson, R. Rodriguez, and A. Emadi, "Jet impingement cooling in power electronics for electrified automotive transportation: Current status and future trends," *IEEE Trans. Power Electron.*, vol. 36, no. 9, pp. 10420–10435, Sep. 2021.

[40] D. J. Womac, S. Ramadhyani, and F. P. Incropera, "Correlating equations for impingement cooling of small heat sources with single circular liquid jets," *J. Heat Transf.*, vol. 115, no. 1, pp. 106–115, Feb. 1993.

[41] D. J. Womac, F. P. Incropera, and S. Ramadhyani, "Correlating equations for impingement cooling of small heat sources with multiple circular liquid jets," *J. Heat Transf.*, vol. 116, no. 2, pp. 482–486, May 1994.

[42] N. R. Saad, S. Polat, and W. J. M. Douglas, "Confined multiple impinging slot jets without crossflow effects," *Int. J. Heat Fluid Flow*, vol. 13, no. 1, pp. 2–14, Mar. 1992.

[43] R. Nadda, A. Kumar, and R. Maithani, "Efficiency improvement of solar photovoltaic/solar air collectors by using impingement jets: A review," *Renew. Sustain. Energy Rev.*, vol. 93, pp. 331–353, Oct. 2018.

[44] A. Sarkar, N. Nitin, M. V. Karwe, and R. P. Singh, "Fluid flow and heat transfer in air jet impingement in food processing," *J. Food Sci.*, vol. 69, no. 4, pp. CRH113–CRH122, May 2004.

[45] F. Tong, W. Gou, Z. Zhao, W. Gao, H. Li, and L. Li, "Numerical investigation of impingement heat transfer on smooth and roughened surfaces in a high-pressure turbine inner casing," *Int. J. Thermal Sci.*, vol. 149, Mar. 2020, Art. no. 106186.

[46] W. Mu et al., "Direct integration of optimized phase-change heat spreaders into SiC power module for thermal performance improvements under high heat flux," *IEEE Trans. Power Electron.*, vol. 37, no. 5, pp. 5398–5410, May 2022.

[47] X. P. Wu et al., "Low profile-high performance vapor chamber heat sinks for cooling high-density blade servers," in *Proc. 23rd Annu. IEEE Semiconductor Thermal Meas. Manage. Symp.*, Mar. 2007, pp. 174–178.

[48] Z. Ming, L. Zhongliang, and M. Guoyuan, "The experimental and numerical investigation of a grooved vapor chamber," *Appl. Thermal Eng.*, vol. 29, nos. 2–3, pp. 422–430, Feb. 2009.

[49] S. N. Joshi et al., "A review of select patented technologies for cooling of high heat flux power semiconductor devices," *IEEE Trans. Power Electron.*, vol. 38, no. 6, pp. 6790–6794, Jun. 2023.

[50] S.-C. Wong, K.-C. Hsieh, J.-D. Wu, and W.-L. Han, "A novel vapor chamber and its performance," *Int. J. Heat Mass Transf.*, vol. 53, nos. 11–12, pp. 2377–2384, May 2010.

[51] Z. Chen, Y. Li, W. Zhou, L. Deng, and Y. Yan, "Design, fabrication and thermal performance of a novel ultra-thin vapour chamber for cooling electronic devices," *Energy Convers. Manage.*, vol. 187, pp. 221–231, May 2019.

[52] H. Zhang, F. Che, T. Lin, and W. Zhao, *Modeling, Analysis, Design, and Tests for Electronics Packaging beyond Moore*. Sawston, U.K.: Woodhead, 2019.

[53] M. Anwar, S. M. N. Hasan, M. Teimor, M. Korich, and M. B. Hayes, "Development of a power dense and environmentally robust traction power inverter for the second-generatio Chevrolet VOLT extended-range EV," in *Proc. IEEE Energy Convers. Congr. Expo. (ECCE)*, Sep. 2015, pp. 6006–6013.

[54] D. J. Sharar, N. R. Jankowski, and B. Morgan, "Thermal performance of a direct-bond-copper aluminum nitride manifold-microchannel cooler," in *Proc. 26th Annu. IEEE Semiconductor Thermal Meas. Manage. Symp. (SEMI-THERM)*, Feb. 2010, pp. 68–73.

[55] S. Yin, K. J. Tseng, and J. Zhao, "Design of AlN-based micro-channel heat sink in direct bond copper for power electronics packaging," *Appl. Thermal Eng.*, vol. 52, no. 1, pp. 120–129, Apr. 2013.

[56] J. Broughton, V. Smet, R. R. Tummala, and Y. K. Joshi, "Review of thermal packaging technologies for automotive power electronics for traction purposes," *J. Electron. Packag.*, vol. 140, no. 4, Dec. 2018, Art. no. 040801.

[57] Y.-H. Peng, D.-H. Wang, X.-Y. Li, and Y. Zhang, "Cooling chip on PCB by embedded active microchannel heat sink," *Int. J. Heat Mass Transf.*, vol. 196, Nov. 2022, Art. no. 123251.

[58] Y. Chen et al., "Direct phase-change cooling of vapor chamber integrated with IGBT power electronic module for automotive application," *IEEE Trans. Power Electron.*, vol. 36, no. 5, pp. 5736–5747, May 2021.

[59] M. Cairnie and C. DiMarino, "Bayesian optimization of PCB-integrated field grading for a high-density 10 kV SiC power module interface," *IEEE Trans. Power Electron.*, vol. 37, no. 7, pp. 7590–7603, Jul. 2022.

[60] L. Han, L. Liang, Z. Zhang, and Y. Kang, "Understanding inherent implication of thermal resistance in double-side cooling module," *IEEE Trans. Power Electron.*, vol. 38, no. 2, pp. 2435–2445, Feb. 2023.

[61] M. Spieler, C.-W. Chang, A. El-Refaie, M. H. Alvi, D. Dong, and R. Burgos, "PCB technology comparison enabling a 900 V SiC MOSFET half bridge design for automotive traction inverters," in *Proc. 24th Eur. Conf. Power Electron. Appl. (EPE ECCE Europe)*, Sep. 2022, pp. 1–11.

[62] J. S. Knoll, G. Son, C. DiMarino, Q. Li, H. Stahr, and M. Morianz, "A PCB-embedded 1.2 kV SiC MOSFET half-bridge package for a 22 kW AC–DC converter," *IEEE Trans. Power Electron.*, vol. 37, no. 10, pp. 11927–11936, Oct. 2022.

[63] L. C. Ordonez, A. D. Exposito, P. A. Cervera, M. Bakic, and T. Wijekoon, "Fast and accurate analytical thermal modeling for planar PCB magnetic components," *IEEE Trans. Power Electron.*, vol. 38, no. 6, pp. 7480–7491, Jun. 2023.

[64] M. Ngo, Y. Cao, D. Dong, R. Burgos, K. Nguyen, and A. Ismail, "Forced air-cooling thermal design methodology for high-density, high-frequency, and high-power planar transformers in 1U applications," *IEEE J. Emerg. Sel. Topics Power Electron.*, vol. 11, no. 2, pp. 2015–2028, Apr. 2023.

[65] Y. Ruan, Y. Cao, D. Dong, and Q. Li, "A high-efficiency modular air-cooling method for PCB winding with the additive manufacturing," in *Proc. IEEE Appl. Power Electron. Conf. Expo. (APEC)*, Mar. 2023, pp. 449–455.

[66] J. Biela and J. W. Kolar, "Cooling concepts for high power density magnetic devices," in *Proc. Power Convers. Conf.*, Nagoya, Japan, Apr. 2007, pp. 1–8.

[67] M. Pavlovsky, S. W. H. de Haan, and J. A. Ferreira, "Design for better thermal management in highpower high-frequency transformers," in *Proc. 14th IAS Annu. Meeting. Conf. Rec. Ind. Appl. Conf.*, Oct. 2005, pp. 2615–2621.

[68] Y. Liu et al., "LCL filter design of a 50-kW 60-kHz SiC inverter with size and thermal considerations for aerospace applications," *IEEE Trans. Ind. Electron.*, vol. 64, no. 10, pp. 8321–8333, Oct. 2017.

[69] J. Xue and F. Wang, "A practical liquid-cooling design method for magnetic components of EMI filter in high power motor drives," in *Proc. IEEE Energy Convers. Congr. Expo. (ECCE)*, Sep. 2016, pp. 1–6.

[70] T. L. Bergman, F. P. Incropera, D. P. DeWitt, and A. S. Lavine, *Fundamentals of Heat and Mass Transfer*. Hoboken, NJ, USA: Wiley, 2011.

[71] S. W. Churchill and H. H. S. Chu, "Correlating equations for laminar and turbulent free convection from a vertical plate," *Int. J. Heat Mass Transf.*, vol. 18, no. 11, pp. 1323–1329, Nov. 1975.

[72] S. Song, V. Au, and K. P. Moran, "Constriction/spreading resistance model for electronics packaging," in *Proc. 4th ASME/JSME Thermal Eng. Joint Conf.*, vol. 4, 1995, pp. 199–206.

[73] R. E. Simons. *A Simple Thermal Resistance Model—Isoflux Versus Isothermal*. Accessed: Jul. 1, 2023. [Online]. Available: https://www.electronics-cooling.com/2006/02/a-simple-thermal-resistance-model-isoflux-versus-isothermal/

[74] *Generic Standard on Printed Board Design*, document IPC-2221A, IPC, Northbrook, IL, USA, 2012.

[75] *Standard for Determining Current-Carrying Capacity in Printed Board Design*, document IPC-2152, IPC, Northbrook, IL, USA, 2009.

[76] X. Zhao et al., "An enhanced modulation scheme for multi-level T-type inverter with loss balance and reduction," *IEEE Trans. Power Electron.*, early access, Jun. 26, 2023, doi: 10.1109/TPEL.2023.3289508.

[77] H. Wen, W. Xiao, X. Wen, and P. Armstrong, "Analysis and evaluation of DC-link capacitors for high-power-density electric vehicle drive systems," *IEEE Trans. Veh. Technol.*, vol. 61, no. 7, pp. 2950–2964, Sep. 2012.

[78] J. Mühlethaler, J. W. Kolar, and A. Ecklebe, "Loss modeling of inductive components employed in power electronic systems," in *Proc. 8th Int. Conf. Power Electron. (ECCE Asia)*, May 2011, pp. 945–952.

[79] X. Zhao, R. Phukan, C. W. Chang, R. Burgos, D. Dong, and P. Asfaux, "Design and optimization of 2 × 211-kW SiC-based aircraft propulsion inverter system with high power density and high efficiency," in *Proc. IEEE Appl. Power Electron. Conf. Expo. (APEC)*, Orlando, FL, USA, Mar. 2023, pp. 1009–1016.

[80] R. Phukan et al., "Enhanced three-phase AC common-mode filter with optimized damping network for VFDs," *IEEE Trans. Ind. Appl.*, vol. 59, no. 4, pp. 4274–4286, Jul./Aug. 2023.

[81] R. Phukan et al., "Characterization and mitigation of conducted emissions in a SiC based three-level T-type motor drive for aircraft propulsion," *IEEE Trans. Ind. Appl.*, pp. 1–14, 2023.

[82] R. Phukan et al., "Optimized DC–AC EMI filter design for DC-fed high speed SiC-based motor drive," in *Proc. IEEE Energy Convers. Congr. Expo. (ECCE)*, Oct. 2022, pp. 1–8.

[83] R. Phukan et al., "A compact integrated DM-CM filter with PCB embedded DC current sensor for high altitude high current applications," in *Proc. IEEE Transport. Electrific. Conf. Expo (ITEC)*, Jun. 2022, pp. 923–928.

[84] B. R. Munson, *Fundamentals of Fluid Mechanics*. Hoboken, NJ, USA: Wiley, 2015.

[85] B. X. Wang and X. F. Peng, "Experimental investigation on liquid forced-convection heat transfer through microchannels," *Int. J. Heat Mass Transf.*, vol. 37, pp. 73–82, Mar. 1994.

[86] X. Zhao et al., "Design of ultracompact gate driver integrated with current sensor and commutation path for a 211-kW three-level SiC aircraft propulsion inverter," *IEEE J. Emerg. Sel. Topics Power Electron.*, vol. 11, no. 4, pp. 4077–4094, Aug. 2023.

[87] X. Zhao, R. Phukan, C.-W. Chang, D. Dong, R. Burgos, and A. Plat, "Design of Rogowski coil current sensor integrated with busbar and gate driver for 211 kW SiC-based three-level T-type inverter," in *Proc. Energy Convers. Congr. Expo. (ECCE)*, Detroit, MI, USA, Oct. 2022, pp. 1–7.

[88] B. Lindgren, J. M. Sterlund, and A. V. Johansson, "Evaluation of scaling laws derived from lie group symmetry methods in zero-pressure-gradient turbulent boundary layers," *J. Fluid Mech.*, vol. 502, pp. 127–152, Mar. 2004.

[89] J. P. Hurtado, B. Villegas, S. Pérez, and E. Acuña, "Optimization study of guide vanes for the intake fan-duct connection using CFD," *Processes*, vol. 9, no. 9, p. 1555, Aug. 2021.

[90] D. Bohne, S. Fischer, and E. Obermeier, "Thermal, conductivity, density, viscosity, and Prandtl-numbers of ethylene glycol-water mixtures," *Berichte der Bunsengesellschaft für Physikalische Chem.*, vol. 88, no. 8, pp. 739–742, Aug. 1984.

[91] X. Zhao et al., "Planar common-mode EMI filter design and optimization for high-altitude 100-kW SiC inverter/rectifier system," *IEEE J. Emerg. Sel. Topics Power Electron.*, vol. 10, no. 5, pp. 5290–5303, Oct. 2022.

Che-Wei Chang (Graduate Student Member, IEEE) received the B.S. degree in electrical engineering from National Sun Yat-sen University (NSYSU), Kaohsiung, Taiwan, in 2017, and the M.S. degree in electrical engineering from National Taiwan University (NTU), Taipei, Taiwan, in 2019. He is currently pursuing the Ph.D. degree in power electronics with the Center for Power Electronics Systems (CPES), Virginia Tech, Blacksburg, VA, USA.

His research interests include paralleling operation and applications of silicon-carbide (SiC) MOSFET and thermal management of traction drive systems.

Mr. Chang was a recipient of the Best Presentation Award at the IEEE Applied Power Electronics Conference (APEC 2023).

Xingchen Zhao (Graduate Student Member, IEEE) received the B.S. and M.S. degrees in electrical engineering from the Nanjing University of Aeronautics and Astronautics (NUAA), Nanjing, China in 2015 and 2018, respectively. He is currently pursuing the Ph.D. degree in power electronics with the Center for Power Electronics Systems (CPES), Virginia Polytechnic Institute and State University, Blacksburg, VA, USA.

His research interests include multilevel inverters, application of silicon-carbide (SiC) devices, integrated sensor design, and electromagnetic interference (EMI) filter design.

Mr. Zhao was a recipient of the Best Paper Award at the 2021 IEEE Energy Conversion Congress and Exposition (ECCE) and the Best Presentation Award at the 2023 IEEE Applied Power Electronics Conference (APEC).

Ripun Phukan (Member, IEEE) received the B.Tech. degree in electrical engineering from SRM University, Chennai, India, in 2013, the M.S. degree in electrical engineering from the Georgia Institute of Technology, Atlanta, GA, USA, in 2016, and the Ph.D. degree in electrical engineering from Virginia Tech, Blacksburg, VA, USA, in 2023.

From 2013 to 2014, he was a Research Associate with IIT, Guwahati, India. From 2016 to 2018, he was an Associate Electrical Engineer with Rockwell Automation, Milwaukee, WI, USA. He is currently a member of the R&D Staff, Delta Power Electronics Laboratory, Delta Electronics (Americas) Ltd., Research Triangle Park, NC, USA. His research interests include high-power-density wide bandgap semiconductor-based power conversion, magnetic integration, electromagnetic interference (EMI) and electromagnetic compatibility (EMC), soft-switching, and multilevel power converters.

Dr. Phukan received the Best Presentation Award at the Applied Power Electronics Conference (APEC 2021), the Honorarium Award at the IEEE Transportation Electrification Conference & Expo (ITEC) in 2022, and the IEEE PELS Ph.D. Thesis Talk Award in 2023.

Rolando Burgos (Senior Member, IEEE) received the B.S. degree in electronics engineering, the Electronics Engineering Professional degree, and the M.S. and Ph.D. degrees in electrical engineering from the University of Concepción, Concepción, Chile, in 1995, 1997, 1999, and 2002, respectively.

In 2002, he joined the Center for Power Electronics Systems (CPES), Virginia Tech, Blacksburg, VA, USA, as a Post-Doctoral Fellow, where he became a Research Scientist in 2003 and a Research Assistant Professor in 2005. In 2009, he joined ABB Corporate Research, Raleigh, NC, USA, where he was a Scientist from 2009 to 2010 and a Principal Scientist from 2010 to 2012. In 2010, he was appointed as an Adjunct Associate Professor at the Electrical and Computer Engineering Department, Future Renewable Electric Energy Delivery and Management (FREEDM) Systems Center, North Carolina State University, Raleigh, NC, USA. In 2012, he returned to Virginia Tech as an Associate Professor at The Bradley Department of Electrical and Computer Engineering, where he earned his tenure in 2017 and was promoted to Professor in 2019. Since 2021, he has been the Director of CPES. His research interests include high-power-density wide bandgap semiconductor-based power conversion, low- and medium-voltage applications, packaging and integration, electromagnetic interference (EMI) and electromagnetic compatibility (EMC), multiphase multilevel power converters, modeling and control, grid power electronics systems, and the stability of ac and dc power systems.

Dr. Burgos is a member of the IEEE Power Electronics Society, the IEEE Industry Applications Society, the IEEE Industrial Electronics Society, and the IEEE Power and Energy Society.

Simon Uicich received the M.S. degree in electrical engineering from the National University of Mar del Plata (UNMDP), Mar del Plata, Argentina, in 2018. He is currently pursuing the Ph.D. degree in power electronics from the Institut National des Sciences Appliquées de Lyon, France.

From 2019 to 2022, he was with the Ampère Laboratory, University of Lyon, Lyon, France, and Airbus, Toulouse, France. He is currently with Airbus working on ZEROe hydrogen propulsion systems. His research interests include converter control, high frequency (HF) magnetics, multidomain electric vehicle (EV) EPU optimization, and power components operation and reliability.

Mr. Uicich was a recipient of the Best Presentation Award at the 2023 Power Electronics for Aerospace Applications—Nottingham Conference (PEASA23).

Pascal Asfaux received the Engineer degree from the École Nationale Supérieure d'Ingénieurs de Limoges (ENSIL), Limoges, France, in 2003.

In 2006, he joined Airbus Company, Toulouse, France, as a Leader in civil and military aerospace products, where he dealt with power electronics design and electromagnetic compatibility (EMC). He currently serves as the Power Electronics Roadmap Owner of Airbus Company. He steers Research and Technology (R&T) projects on power electronics in all divisions to develop group-wide synergies and to align with top-level CTO objectives. He develops, manages, coordinates, and matures the technology roadmap, creating a vision. He serves as the power electronics project leader too. He works closely with design office teams to assess and integrate new power electronics technologies into next-generation aircraft systems. He has been working in the field of power electronics for over 15 years in the frame of R&T projects.

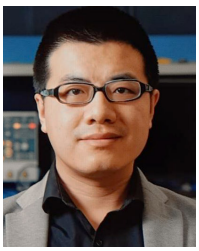

Dong Dong (Senior Member, IEEE) received the B.S. degree in electrical engineering from Tsinghua University, Beijing, China, in 2007, and the M.S. and Ph.D. degrees in electrical engineering from Virginia Tech, Blacksburg, VA, USA, in 2009 and 2012, respectively.

From 2012 to 2018, he was an Electrical Engineer with the GE Global Research Center (GRC), Niskayuna, NY, USA. Since 2018, he has been with The Bradley Department of Electrical and Computer Engineering, Virginia Tech. He has published over 60 refereed journal publications and more than 100 IEEE conference publications. He currently holds 36 granted U.S. patents. His research interests include wide bandgap power semiconductor-based high-frequency power conversion, soft-switching and resonant converters, high-frequency transformers, and medium-voltage (MV) and high-voltage (HV) power conversion systems for grid, renewable, and transportation applications.

Dr. Dong received multiple technology awards, including the GE Silver and Gold Medallion Patent Awards and the GE Technology Transition Awards. He received four Transaction Prize Paper Awards from the IEEE TRANSACTIONS ON POWER ELECTRONICS, IEEE TRANSACTIONS ON INDUSTRY APPLICATIONS, and IEEE JOURNAL OF EMERGING AND SELECTED TOPICS IN POWER ELECTRONICS, the IEEE William Portnoy Prize Paper Award, the IEEE Transportation Systems Prize Paper Award from IEEE Industry Applications Society (IAS), one Best Paper Award from IEEE Energy Conversion Congress and Exposition (ECCE)-Asia, one Prize Paper Award from IEEE International Power Electronics Conference (IPC), the First Place of ECCE Hardware Demo, and the NSF CAREER Award. He has served as the Vice-Chair of the IEEE Industry Application Society Schenectady Region Chapter in 2017 and the IEEE Power Electronics Society (PELS) Technical Committees (TC) 1: Control and Modeling of Power Electronics, and the General Chair of IEEE International Conference on DC Microgrids in 2021.